Monthly Notices of the ROYAL ASTRONOMICAL SOCIETY

MNRAS **515,** 4622–4638 (2022) https://doi.org/10.1093/mnras/stac2005
Advance Access publication 2022 July 22

On the accretion of a new group of galaxies on to Virgo – II. The effect of pre-processing on the stellar population content of dEs

Bahar Bidaran,[1]★ Francesco La Barbera [2],[2] Anna Pasquali [1]★,[1]★ Reynier Peletier [3],[3] Glenn van de Ven [4],[4] Eva K. Grebel,[1] Jesus Falcón-Barroso,[5,6] Agnieszka Sybilska,[7] Dimitri A. Gadotti [8,9] and Lodovico Coccato [8]

[1]*Astronomisches Rechen-Institut, Zentrum für Astronomie der Universität Heidelberg, Mönchhofstraße 12-14, D-69120 Heidelberg, Germany*
[2]*INAF – Osservatorio Astronomico di Capodimonte, Salita Moiariello 16, I-80020 Napoli, Italy*
[3]*Kapteyn Astronomical Institute, University of Groningen, Postbus 800, NL-9700 AV Groningen, the Netherlands*
[4]*Department of Astrophysics, University of Vienna, Türkenschanzstrasse 17, A-1180 Vienna, Austria*
[5]*Instituto de Astrofísica de Canarias, Calle Vía Láctea s/n, E-38205 La Laguna, Tenerife, Spain*
[6]*Departamento de Astrofísica, Universidad de La Laguna, , E-38200 La Laguna, Tenerife, Spain*
[7]*Sybilla Technologies, Torunska 59, PL-85-023 Bydgoszcz, Poland*
[8]*European Southern Observatory, Karl-Schwarzschild-Str 2, D-85748 Garching, Germany*
[9]*Centre for Extragalactic Astronomy, Department of Physics, Durham University, South Road, Durham DH1 3LE, UK*

Accepted 2022 July 13. Received 2022 July 13; in original form 2022 May 19

ABSTRACT

Using MUSE spectra, we investigate how pre-processing and accretion on to a galaxy cluster affect the integrated stellar population properties of dwarf early-type galaxies (dEs). We analyse a sample of nine dEs with stellar masses of $\sim 10^9\,M_\odot$, which were accreted ($\sim$ 2–3 Gyr ago) on to the Virgo cluster as members of a massive galaxy group. We derive their stellar population properties, namely age, metallicity ([M/H]), and the abundance ratio of α elements ([α/Fe]), by fitting observed spectral indices with a robust, iterative procedure, and infer their star formation history (SFH) by means of full spectral fitting. We find that these nine dEs are more metal-poor (at the 2–3σ level) and significantly more α-enhanced than dEs in the Virgo and Coma clusters with similar stellar mass, clustercentric distance, and infall time. Moreover, for six dEs, we find evidence for a recent episode of star formation during or right after the time of accretion on to Virgo. We interpret the high [α/Fe] of our sample of dEs as the result of the previous exposure of these galaxies to an environment hostile to star formation, and/or the putative short burst of star formation they underwent after infall into Virgo. Our results suggest that the stellar population properties of low-mass galaxies may be the result of the combined effect of pre-processing in galaxy groups and environmental processes (such as ram-pressure triggering star formation) acting during the early phases of accretion on to a cluster.

Key words: galaxies: dwarf – galaxies: evolution – galaxies: interactions – galaxies: star formation.

1 INTRODUCTION

Early-type dwarf galaxies (dEs) are low-mass and low-surface brightness systems (with $M_B \geq -18$ mag) that are particularly abundant in high-density regions of the Universe, such as galaxy groups and clusters (Oemler 1974; Dressler 1980; Postman & Geller 1984; Whitmore, Gilmore & Jones 1993; Kauffmann et al. 2004; Peng et al. 2010; Davies et al. 2019). These galaxies are generally dominated by metal-poor stellar populations (with [M/H] < 0.00 [dex]) that cover a rather wide range of light-weighted ages ($3 <$ age [Gyr] < 14). Most of the dEs observed to date are dominated by solar-scaled [α/Fe] abundance ratios (Geha, Guhathakurta & van der Marel 2003; van Zee, Skillman & Haynes 2004; Paudel et al. 2010; Şen et al. 2018). The level of [α/Fe] enhancement in dEs is similar to the high-metallicity stars of the Milky Way (MW) and the Large Magellanic Cloud (LMC; Sybilska et al. 2018).

★ E-mail: bidaran@uni-heidelberg.de (BB); pasquali@ari.uni-heidelberg.de (AP)

Dwarf elliptical galaxies show diverse morphologies, dynamics, and stellar population properties. For instance, in the core of clusters, dEs are often old, metal-poor, and slow-rotating systems (e.g. Geha et al. 2006; Koleva et al. 2009; Toloba et al. 2011, 2014; Ryś, van de Ven & Falcón-Barroso 2014; Sybilska et al. 2017; Scott et al. 2020). In the Lambda cold dark matter (ΛCDM) framework (Cole et al. 2000) of hierarchical structure formation, dEs might have formed from protogalaxies in the early Universe and ever since evolved passively (e.g. De Rijcke et al. 2003; Wheeler et al. 2017). None the less, the presence of disc features (Lisker, Grebel & Binggeli 2006a; Lisker et al. 2006b), stripped tails of H I gas, and prolonged star formation history akin to that of low-mass late-type star-forming galaxies, challenge the picture presented above. Therefore, Kormendy (1985) suggested the transformation of late-type star-forming galaxies under environmental effects as another possible formation channel for part of the present-day dEs in clusters and galaxy groups (also check Binggeli, Sandage & Tammann 1988; Lisker et al. 2013; Boselli & Gavazzi 2014).

Within a massive host halo, ram pressure stripping (RPS) exerted by the intracluster medium can effectively exhaust the star formation

activity of satellites by depleting their cold gas reservoir over a short time-scale of ∼1 Gyr (Gunn & Gott 1972; Hester et al. 2010; Fumagalli et al. 2011; Kenney et al. 2014; Boselli, Fossati & Sun 2021; Roberts et al. 2021). Ram pressure can also trigger local star formation enhancements, as a result of gas compression in the leading part and core of infalling satellites (e.g. Lee et al. 2017; Fossati et al. 2018; Boselli et al. 2021) (but see: Mun et al. 2021). Furthermore, the gravitational potential well of the host halo and multiple close encounters with other halo members apply tidal forces on satellites over a time-scale of several Gyr, and are thus able to modify their dynamics, morphology, and star formation history. These tidal interactions are known as galaxy strangulation (Larson, Tinsley & Caldwell 1980) and harassment, respectively (Moore et al. 1996; Moore, Lake & Katz 1998; Boselli & Gavazzi 2006). Hence we expect to find correlations between the properties of dEs (i.e. their morphologies, dynamics, colours, and stellar populations) and their local density, host halo mass, and cluster-centric distance.

Observations have shown that red and quenched dEs make up a large galaxy population in clusters and massive galaxy groups (Chilingarian et al. 2008; Smith et al. 2009; Lisker et al. 2013; Sybilska et al. 2017; Janz et al. 2021; Su et al. 2021; Venhola et al. 2021). The fraction of old and quenched low-mass galaxies increases with the host halo mass, as observed by Pasquali et al. (2010) and Gallazzi et al. (2021). Within a massive host halo, however, their relative number decreases towards larger cluster-centric distances (Chilingarian et al. 2008; Smith et al. 2009; Lisker et al. 2013). For instance, in the Coma cluster, Smith et al. (2009) showed that the population of young (∼3 Gyr) dEs with solar-scaled [Mg/Fe] abundance ratios increases towards the cluster outskirts. They also found that in the core of Coma, dEs are mostly old (∼10 Gyr) and Mg-enhanced. A similar behaviour is also observed in Abell 496 by Chilingarian et al. (2008) and in Virgo by Liu et al. (2016). Such observed trends emphasize the role of environment in transforming its low-mass satellite galaxies.

None the less, such a transformation may start long before dEs are accreted on to their current host halo. According to the ΛCDM framework, clusters grow through the accretion of galaxies, either individually or in pairs and more populated groups where they may have already experienced environmental effects. This is known as pre-processing (Fujita 2004; Mihos 2004) and can for example explain the presence of gas-deprived galaxies or galaxies with a low star formation rate, as well quenched galaxies beyond the cluster virial radius (Kodama & Smail 2001; Lewis et al. 2002; Mahajan, Raychaudhury & Pimbblet 2012; Haines et al. 2015; Donnari et al. 2021) Distinguishing between the effects of pre-processing and the effects of the current host halo is, however, not straightforward, since their differences dilute through time. One possible way to disentangle current halo processing from pre-processing can be the study of newly accreted dEs in dynamically young galaxy clusters like Virgo.

In the projected phase-space diagram of ∼620 Virgo galaxies, Lisker et al. (2018) discovered a sample of nine dEs (with $-17 \geq M_r\ [mag] > -18$) that according to *N*-body simulations of Vijayaraghavan, Gallagher & Ricker (2015) should have recently been accreted on to Virgo as gravitationally bound members of a massive galaxy group (with $M_\star/M_\odot \sim 10^{13}$). According to the simulations, this infall occurred along the observer's line of sight about 2–3 Gyr ago. In Bidaran et al. (2020) (hereafter B20), we confirmed this relatively recent infall time using the results of Pasquali et al. (2019) and Smith et al. (2019) who dissected the projected phase-space diagram into several zones of different average infall time. In B20, we conducted a kinematic analysis of these nine dEs based on Multi-Unit Spectroscopic Explorer (MUSE) data and showed that, despite their similar stellar mass range and infall time to Virgo, they feature diverse kinematic properties. In particular, we showed that their specific angular momentum (λ_R) profiles are intermediate between equally massive star-forming galaxies in the field and equally massive Virgo dEs with earlier infall times. We interpreted this diversity in their λ_R profiles as possible footprints of pre-processing in their previous group environment. On these grounds, we would expect to detect the effects of such pre-processing also in their stellar population properties.

In this study, we use the MUSE spectra of B20 to derive the integrated stellar population properties and star formation history of our sample of dEs. In order to disentangle group pre-processing from cluster early processing, we also compare our sample with other Virgo and Coma dEs within a similar stellar mass range and infall time. The latter is estimated using the position of cluster dEs in the projected phase-space diagram of their host haloes (Pasquali et al. 2019; Smith et al. 2019). The results of this investigation can also help to understand how dense environments, such as the Virgo cluster, alter the stellar population properties of their satellites during their accretion event and early phases of infall.

This paper is organized as follows: In Section 2, we briefly introduce our main sample and the comparison samples that we use in our analysis. In Section 3, we describe the methods that we utilize for deriving stellar population parameters from the MUSE cubes of our main sample. In Section 4, we present the integrated stellar population properties and star formation histories of our sample, and compare them with those of the comparison samples. We discuss our results in Section 5 and summarize them in Section 6.

2 DATA

2.1 Our sample

We analyse the integrated stellar population properties for the sample of nine Virgo dEs ($-17 \geq M_r\ [mag] > -18$) studied by B20, where their selection criteria are presented and the data reduction is described. Briefly, we observed these galaxies using the MUSE instrument mounted on the Very Large Telescope (VLT), following a science verification proposal in the period of 2016 December to 2017 February, and 2018 February–2018 July (P98, ESO programs 098.B-0619 and 0100.B-0573; PI: Lisker). Our MUSE data set maps a field of view of 1×1 arcmin^2 with a spatial resolution of 0.2 arcsec pixel^{-1}. The spectral resolution of MUSE is wavelength dependent and its average full width at half maximum (FWHM) is 2.5 Å (Bacon et al. 2010). MUSE spectra cover the optical wavelength range from 4750 to 9350 Å. All dEs in our sample were observed with a nearly constant seeing (mean FWHM ∼ 1.6 arcsec).

We summarize the properties of our sample of dEs in Table 1 where we list the name of our target, their morphological type, coordinates, redshift, *r*-band effective radius, absolute *r*-band magnitude, $g - r$ colour, foreground Galactic extinction in the *V* band (A_V), stellar velocity dispersion at 1 effective radius (R_e), specific angular momentum at $1R_e$ (λ_{Re}), and total exposure time (TET) of the MUSE observations. All the reported values, except for A_V, λ_{Re}, and σ_{Re}, are taken from Lisker et al. (2006a). For each dE, the A_V value is taken from Schlafly & Finkbeiner (2011) through the NASA/IPAC Extragalactic Database (NED). The values of λ_{Re} and σ_{Re} for each dE are taken from B20. The absolute *r*-band magnitudes and colours

Table 1. Properties of our dEs.

Object	type	α (J2000)	δ (J2000)	z^a	R_e^a (arcsec)	M_r^a (mag)	g–r^a (mag)	A_V^b (mag)	σ_{Re}^c (km s^{-1})	λ_{Re}^c	TET (h)
VCC 0170	dE(bc)	12 15 56.30	+14 25 59.2	0.00472	31.″57	−17.62	0.59	0.089	27.1 ± 10.6	0.45 ± 0.03	4
VCC 0407	dE(di)	12 20 18.80	+09 32 43.1	0.00626	18.″38	−17.37	0.61	0.057	32.3 ± 8.8	0.67 ± 0.03	2
VCC 0608	dE(di)	12 23 01.70	+15 54 20.2	0.00607	25.″77	−17.58	0.60	0.072	25.1 ± 9.2	0.38 ± 0.04	5
VCC 0794	dE(nN)	12 25 21.61	+16 25 46.9	0.00558	37.″33	−17.29	0.61	0.065	33.0 ± 7.5	0.48 ± 0.04	3
VCC 0990	dE(di)	12 27 16.93	+16 01 28.1	0.00573	10.″31	−17.43	0.62	0.080	36.0 ± 5.6	0.27 ± 0.03	3
VCC 1833	–	12 40 19.70	+15 56 07.1	0.00569	8.″52	−17.44	0.61	0.099	34.4 ± 6.0	0.15 ± 0.06	1.5
VCC 1836	dE(di)	12 40 19.50	+14 42 54.0	0.00668	42.″27	−17.45	0.58	0.079	38.5 ± 8.2	0.55 ± 0.03	4
VCC 1896	dE(di)	12 41 54.60	+09 35 04.9	0.00629	14.″98	−17.04	0.62	0.047	27.0 ± 7.2	0.22 ± 0.04	3
VCC 2019	dE(di)	12 45 20.40	+13 41 34.1	0.00607	18.″60	−17.65	0.63	0.060	31.2 ± 6.5	0.73 ± 0.05	2

Notes.Notes. The columns show: Name of target, morphological type, right ascension and declination, redshift (z), effective radius (R_e) measured at the half-light major axis, absolute r-band magnitude (M_r), g–r colour measured at $1R_e$, foreground Galactic extinction in the V band (A_V), stellar velocity dispersion at $1R_e$ (σ_{Re}), specific angular momentum at $1R_e$ (λ_{Re}), total exposure time (TET).
[a]Lisker et al. (2006a).
[b]Schlafly & Finkbeiner (2011).
[c] Bidaran et al. (2020).

were corrected for Galactic foreground extinction by Lisker et al. (2006a) and Janz & Lisker (2008, 2009). As estimated in B20, our dEs fall in the stellar mass range of $8.9 < \log(M_\star\ [M_\odot]) < 9.2$.

2.2 The comparison samples

In this study, we compare our results with those for other dEs in the Virgo and Coma clusters with $-17 \geq M_r\ [\mathrm{mag}] \geq -18$.[1] This cut in absolute magnitude corresponds to a narrow mass range that allows us to investigate environmental effects at fixed stellar mass. The comparison samples include the following dEs from the literature:

(i) 8 Virgo dEs from Toloba et al. (2014) and 6 Virgo dEs from Şen et al. (2018). The stellar population properties of these galaxies were obtained from long-slit spectra (observed with three different telescopes: William Herschel Telescope, Isaac Newton Telescope, and VLT using the FORS2 spectrograph).
(ii) 4 Virgo dEs from Paudel et al. (2010). Their stellar population properties were derived using long-slit spectra acquired with the FORS2 spectrograph on the VLT.
(iii) 13 Virgo dEs from Sybilska et al. (2017). The stellar population properties of these galaxies were measured using IFU spectra obtained with the SAURON spectrograph at the William Herschel Telescope.
(iv) 47 Coma dEs from Smith et al. (2009). Their stellar population properties were determined using long-slit spectra from the Hectospec fiber-fed spectrograph at the MMT telescope.
The addition of the Coma dEs to the Virgo comparison sample compensates for the fact that measurements of the [α/Fe] ratio for Virgo dEs are quite scarce. Moreover, it also can remedy possible biases due to Virgo being a dynamically young galaxy cluster with substructures, which may not fully show up in the projected phase-space diagram as we define it. Thus, adding the Coma cluster, which is more relaxed than Virgo, can be beneficial for generalizing observed trends in our study.

Throughout this paper, we refer to the dEs of the comparison samples that belong to the Coma and Virgo clusters as the 'Coma dEs' and 'Virgo dEs', respectively. All dEs in both clusters and including our sample dEs are referred to as the 'cluster dEs', whenever needed.

[1]We assume a distance of 16.5 Mpc to the Virgo cluster (e.g. Mei et al. 2007) and 100 Mpc to the Coma cluster (e.g. Carter et al. 2008).

3 ANALYSIS

3.1 Setup and pre-processing of the data

We mask the non-related background galaxies and foreground stars in each dE MUSE datacube. We then construct the integrated MUSE spectrum by averaging each dE datacube within $1R_e$, where spaxels with SNR < 3 have been discarded. We use the Galactic extinction law of Cardelli, Clayton & Mathis (1989) to correct these integrated spectra for Galactic foreground extinction. Here we adopt $R_v = 3.10$ and the A_V values as reported in Table 1. Additionally, we correct the spectra for possible nebular emission lines. As discussed in B20, we have detected relatively strong nebular emission lines (i.e. Hβ, Hα, [O III], [N II], and [S II]) in the central regions of VCC0170. We perform the emission line correction for all dEs in our MUSE sample, using the Gas AND Absorption Line Fitting (GANDALF; Falcón-Barroso et al. 2006; Sarzi et al. 2006) package. This software treats each emission line as a Gaussian function, and simultaneously fits the stellar continuum and emission lines. The observed spectrum is corrected by subtracting the resulting residual emission line spectrum obtained for the best fit. We use these corrected integrated spectra to measure line indices, and later to determine the stellar population properties, as well as star formation histories of our dEs.

In this study, we use single stellar population (SSP) models of Vazdekis et al. (2010, 2015) based on the MILES stellar library (Sánchez-Blázquez et al. 2006; Cenarro et al. 2007; Falcón-Barroso et al. 2011). These SSP models span the age range of 0.5–14.0 Gyr, the metallicity range of −1.26 to 0.06 dex, and the [α/Fe] values of 0.00 dex (solar-scaled models) and 0.40 dex (α-enhanced models). The SSPs were constructed using BASTI isochrones (Pietrinferni et al. 2004) and a bi-modal initial mass function (IMF) with a slope of 1.3 (Vazdekis et al. 1996). We broaden them from their original spectral resolution (FWHM = 2.51 Å) to FWHM = 5 Å, i.e. the LIS-5 Å system (Vazdekis et al. 2010), which is consistent with the typical velocity dispersion of dEs.

3.2 Line-strength measurements

To derive SSP-equivalent stellar ages, metallicities, and [α/Fe] ratios, we use the set of line indices defined in Table A1, where the Hβ and Hβ_0 indices are age-sensitive, and the Fe5015, Mgb5177, Fe5270, and Fe5335 indices are sensitive to metallicity. The indices are measured after smoothing all observed spectra to the 5 Å resolution

Table 2. Measured indices and SSP-equivalent properties of our dEs within $1R_e$.

Object	H β (Å)	H β_0 (Å)	Mgb (Å)	Fe5015 (Å)	Fe5270 (Å)	Fe5335 (Å)	[MgFe] (Å)	< Fe > (Å)	Age (Gyr)	[M/H] (dex)	[α/Fe] (dex)
VCC 0170	3.39 ± 0.08	4.50 ± 0.17	1.60 ± 0.11	2.75 ± 0.25	1.71 ± 0.09	1.49 ± 0.21	1.62 ± 0.07	1.60 ± 0.11	$2.10^{+0.16}_{-0.38}$	$-0.61^{+0.04}_{-0.04}$	$0.26^{+0.09}_{-0.08}$
VCC 0407	2.70 ± 0.07	3.63 ± 0.12	1.89 ± 0.11	3.59 ± 0.22	2.01 ± 0.11	1.83 ± 0.18	1.92 ± 0.07	1.92 ± 0.10	$5.78^{7.34}_{-1.02}$	$-0.59^{+0.06}_{-0.06}$	$0.20^{+0.08}_{-0.08}$
VCC 0608	2.79 ± 0.14	3.79 ± 0.09	1.89 ± 0.17	3.58 ± 0.23	1.95 ± 0.13	1.77 ± 0.09	1.89 ± 0.10	1.86 ± 0.08	$4.55^{+1.06}_{-0.53}$	$-0.57^{+0.06}_{-0.08}$	$0.22^{+0.08}_{-0.08}$
VCC 0794	2.12 ± 0.09	2.89 ± 0.07	1.86 ± 0.08	2.81 ± 0.18	1.75 ± 0.15	1.50 ± 0.20	1.77 ± 0.07	1.62 ± 0.12	$9.98^{0.31}_{-0.40}$	$-0.73^{+0.02}_{-0.02}$	$0.43^{+0.06}_{-0.08}$
VCC 0990	2.37 ± 0.12	3.40 ± 0.17	2.28 ± 0.20	4.17 ± 0.20	2.29 ± 0.12	2.00 ± 0.09	2.14 ± 0.09	2.18 ± 0.11	$7.77^{+3.59}_{-1.59}$	$-0.53^{+0.06}_{-0.06}$	$0.14^{+0.08}_{-0.08}$
VCC 1833	2.78 ± 0.10	3.85 ± 0.11	2.31 ± 0.10	4.36 ± 0.24	2.30 ± 0.13	2.00 ± 0.10	2.19 ± 0.09	2.14 ± 0.11	$3.66^{+1.28}_{-1.06}$	$-0.37^{+0.12}_{-0.08}$	$0.19^{+0.08}_{-0.08}$
VCC 1836	2.81 ± 0.14	3.71 ± 0.11	1.57 ± 0.09	3.14 ± 0.14	1.77 ± 0.09	1.56 ± 0.13	1.64 ± 0.06	1.66 ± 0.08	$6.84^{+5.96}_{-2.25}$	$-0.77^{+0.08}_{-0.06}$	$0.28^{+0.04}_{-0.06}$
VCC 1896	2.16 ± 0.09	3.04 ± 0.12	2.19 ± 0.07	3.55 ± 0.16	2.04 ± 0.10	1.95 ± 0.09	2.10 ± 0.05	1.99 ± 0.07	$10.50^{0.48}_{-0.53}$	$-0.59^{+0.02}_{-0.02}$	$0.26^{+0.04}_{-0.06}$
VCC 2019	2.34 ± 0.09	3.07 ± 0.15	2.17 ± 0.07	3.71 ± 0.14	2.09 ± 0.10	1.87 ± 0.07	2.10 ± 0.05	1.98 ± 0.06	$10.46^{0.48}_{-1.02}$	$-0.59^{+0.04}_{-0.02}$	$0.26^{+0.04}_{-0.04}$

Note. The columns show: (1) Target name, (2–9) measured indices and their corresponding errors, (10–12) light-weighted age, metallicity, and [α/Fe]. All the values are measured using the dEs' integrated MUSE spectra.

of the LIS-5 Å system (Vazdekis et al. 2010). The convolution is based on a Gaussian kernel whose $\mathrm{FWHM_{final}}$ is defined as

$$\mathrm{FWHM_{final}} = \sqrt{\mathrm{FWHM^2_{LIS5.00}} - (\mathrm{FWHM^2_{MUSE}} + \mathrm{FWHM^2_{\sigma}})}, \quad (1)$$

where $\mathrm{FWHM_{MUSE}}$ is the wavelength-dependent MUSE resolution (Bacon et al. 2017) and $\mathrm{FWHM_{\sigma}}$ corresponds to the stellar velocity dispersion of each dE as reported in Table 1.

To estimate the random error on each measured index, we consider three possible uncertainty sources: the error on the stellar velocity dispersion (affecting the absorption line width), the error on the redshift estimate (affecting the accurate placement of the index band-passes), and the error on the spectral flux (Kuntschner et al. 2006). Thus, we perturb the flux values in the spectra using a Gaussian distribution with width equal to the estimated flux errors. Furthermore, we randomly shift the perturbed spectra using a normal Gaussian distribution of redshift errors. Additionally, in each perturbation, we change the convolution kernel size by randomly shifting the stellar velocity dispersion within a normal distribution constructed on the corresponding σ errors. Based on this error treatment, we run 125 Monte Carlo (MC) iterations for each spectrum and assume the standard deviation of the multiple measurements of each index as its corresponding error. Furthermore, we notice that since stellar population models have their own uncertainties, matching observed and model line strengths for high S/N ratio spectra may lead to unrealistically small errors on stellar population parameters. Indeed, using spectral fitting (with the software STARLIGHT), we estimated that the quality of the fits to our MUSE spectra does not improve significantly when S/N is larger than ∼150, corresponding to a typical uncertainty of ∼0.05 Å for the line strengths we analyse in this work. Therefore, we decided to add a minimum uncertainty of 0.05 Å in quadrature to the errors on observed line strengths. The measured indices and their uncertainties for our sample of dEs are reported in Table 2.

In the top panel of Fig. 1, we compare the H β_0 and [MgFe] indices measured from the integrated spectrum of each dE (colour-coded circles) with SSP predictions (black grid, corresponding to SSPs with [α/Fe] = 0.40 dex). The metallicity-sensitive and composite [MgFe] index is derived as in Thomas, Maraston & Bender (2003):

$$[\mathrm{MgFe}] = \sqrt{\mathrm{Mgb} \times (0.72 \times \mathrm{Fe5270} + 0.28 \times \mathrm{Fe5335})}. \quad (2)$$

The diagonal lines of the grid have constant metallicity (from left to right: −1.26, −0.96, −0.35, −0.25, and 0.06 dex), while the horizontal lines have constant age (from top to bottom: 1.5, 4.0, 8.0,

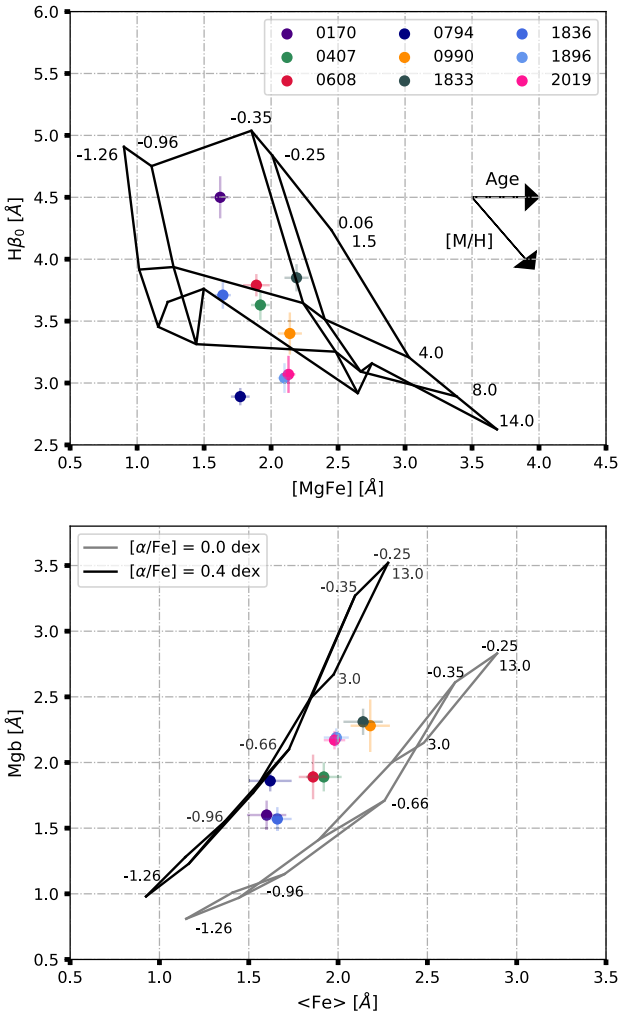

Figure 1. *Top panel*: The H β_0 versus [MgFe] grid. SSP model predictions with [α/Fe] = 0.4 dex are plotted with black solid lines. Following the horizontal arrow from left to right, metallicity increases along the grid from −1.26 to +0.06 dex. Similarly, as shown by the diagonal arrow and from top to bottom, age increases from 1.5 to 14 Gyr. *Lower panel*: *The Mgb versus* < Fe > *grid. Model predictions with [α/Fe] = 0.00 and 0.4 dex for two ages (3.0 and 13 Gyr) and the metallicity range of [−1.26, −0.96, −0.66, −0.35, −0.25] dex are shown with grey and black solid lines, respectively. In both panels, our dEs are denoted with colour-coded circles as listed in the legend in the top panel.*

and 14 Gyr). The distribution of our dEs in H β_0 versus [MgFe] indicate that they span quite a range of ages.

We plot the Mgb and <Fe> indices of our dEs (with <Fe> being the average of Fe5270 and Fe5335) in the bottom panel of Fig. 1, together with two SSP grids corresponding to [α/Fe] = 0.00 dex and 0.40 dex, in grey and black, respectively. Each grid shows the SSP predictions for the ages of 3.0 and 13.0 Gyr and the metallicity range of [−1.26, −0.96, −0.66, −0.35, and -0.25] dex. Note that in this work, we use Mgb5177 as a proxy for α abundance. We notice that our dEs follow a quite tight distribution on this plane, being systematically and consistently α-enriched.

3.3 SSP-equivalent properties

In order to fit the observed indices with those provided by the SSP models, we construct finer grids of SSP predictions, by linearly interpolating the SSP models in age-[M/H]–[α/Fe]-[index] space, using steps of 0.02 and 0.015 dex in metallicity and [α/Fe], respectively. For what concerns the interpolation in age, one should consider that variations in age are much larger for young ages (0.5 < age [Gyr] < 3) relative to old ones (3 < age [Gyr] < 14). Hence, to keep the number density of models approximately constant over the SSPs' age range, we adopt age steps of 0.01 and 0.04 Gyr for young and old ages, respectively. As shown in the bottom panel of Fig. 1, a couple of galaxies are quite close to the black grid of SSPs with [α/Fe] = 0.4 dex, the maximum value for which models were computed. This may raise concerns regarding false parameter estimates and systematic errors. Moreover, the [α/Fe] of Coma and Virgo dEs from Smith et al. (2009) and Sybilska et al. (2017) span a range of ∼[−0.3,0.6] dex. Therefore, we decide to also extrapolate the SSP models in steps of 0.015 dex to fill a final [α/Fe] range of −0.3 to 0.7 dex.

To translate the measured indices into model-predicted stellar population properties, we employ a χ^2 minimization approach in four steps, each time fitting over certain index pairs:

Step 1: we construct the finer H β_0–[MgFe] grid for solar-scaled SSP models. Based on the galaxy position in this grid, we fit the SSP-equivalent age by running the χ^2 minimization method. We construct the probability distribution function (PDF) of age in this step by repeating the fitting procedure 25 times in an MC framework. In each MC run, we shift the measured indices accounting for their errors. The resulting age PDF is used in the next step.

Step 2: we construct the finer Mgb-<Fe> grid using models at values randomly selected from the age PDF delivered by Step 1. Then, we measure the [α/Fe] PDF from 100 MC realizations, each based on the χ^2 minimization method. We repeat this test for 50 randomly selected values from the age PDF. The final [α/Fe] PDF, which is passed to Step 3, is the average of all these 50 random selections.

Step 3: we randomly select 100 values from the [α/Fe] PDF delivered by Step 2, and execute 200 MC iterations for each selected value. Here, we revisit the finer H β_0–[MgFe] grid, each time constructed for a randomly selected [α/Fe] value from the [α/Fe] PDF of Step 2. The reason why we repeat this step (with respect to Step 1), is to account for the dependence of H β_0 on [α/Fe] (see Vazdekis et al. 2015). The final age (in Gyr) and [M/H] (in dex) are measured as the median of their corresponding PDFs constructed by the end of Step 3.

Step 4: as the last step, we repeat the same methodology of Step 2 by randomly selecting 100 ages from the age PDF of Step 3 and executing 200 MC iterations for each selected age. The final [α/Fe] value (in dex) is measured as the median of the resulting PDF in this step.

In our iterative fitting approach, each stellar population parameter is derived based on the absorption features to which it is more sensitive to. An alternative approach would be performing simultaneous fits over the parameter space, where a combination of absorption features with different levels of sensitivity is taken into account. Here, we choose to apply an iterative index fitting approach to gain more robust results. In the last three columns of Table 2, we report the integrated stellar population parameters of our dEs, measured as medians of PDFs from Steps 3 and 4. The reported errors are the 84th and 16th percentiles of the final PDFs. It should be noted that the stellar population properties in Table 2 are light-weighted values. Since the recent formation of even a few young and hot stars in galaxies can affect their composite light drastically, our measurements might be biased toward the recent star formation in these galaxies, if any. However, the effect is not expected to be severe for [M/H] results, as the contribution of hot and young stars to metal lines of the integrated spectra is not significant (Trager et al. 2005; Serra & Trager 2007).

3.4 Full spectrum fitting using STARLIGHT

To investigate the star formation histories of our sample of dEs, we utilize the publicly available full-spectrum fitting routine STARLIGHT.[2] STARLIGHT constructs the best-fitting synthetic spectrum by linearly combining a set of SSP models with different ages and metallicities (Cid Fernandes et al. 2005). We perform the full spectrum fitting over the integrated spectra of our dEs to measure their light- and mass-weighted stellar population properties. Since full-spectrum fitting does not consider a single SSP (as in our index fitting approach), but a combination of SSP models, it provides an additional and complementary estimate of the stellar populations content of our dEs. Furthermore, we use the STARLIGHT population vectors (the fraction of either light or mass contributed by each SSP to the best-fitting synthetic spectrum) to build the star formation histories of our dEs.

We perform the fitting over the spectral range of 4750–5540 Å. This wavelength range contains the most crucial absorption features that are sensitive to age and [M/H] and is less affected by telluric lines (for more explanation on possible impacts of selected wavelength ranges on the results of full-spectrum fitting, see: Gonçalves et al. 2020). To normalize the input flux, STARLIGHT uses the median of the observed spectrum in a specific user-defined wavelength range, called the 'S/N window'. We define our preferred S/N window in the wavelength range of 4750–4800 Å.

In order to compare the results of STARLIGHT with those of the Lick indices fitting, we run STARLIGHT using the same set of SSP models as for index fitting (i.e. same IMF and isochrones, see Section 3.1). In STARLIGHT, we use SSP models in the age range of 1–14 Gyr (with Δ_{age} = 1 Gyr) and the metallicity range of −1.26 to −0.25 dex. As explained in Section 3.3, absorption features that are present in our adopted fitting wavelength range are not only age and [M/H] dependent but also are sensitive to [α/Fe]. As discussed in Vazdekis et al. (2015), the full spectrum fitting does not correctly estimate [α/Fe] ratios, unless a narrow wavelength range around the Mgb absorption feature is selected. On the other hand, STARLIGHT only accepts a limited number of SSP models as its defined stellar base (up to 300). Thus, we adopt a simplified approach where [α/Fe] is fixed to the value derived with the index fitting method (i.e. values in Table 2).

[2] http://www.starlight.ufsc.br/

To do so, we linearly interpolate the flux of the SSP models with similar age and [M/H], but different [α/Fe], at each wavelength. Hence, we construct new SSP models with different levels of α-enrichment. Per [α/Fe] value, we name this new set of models as a new 'SSP family'. In the case of VCC0794, the most α-enhanced dE in our sample with [α/Fe] = 0.43 dex, the desired SSP family is constructed by linearly extrapolating the available SSP models beyond their maximum value of 0.4 dex. To fit each dE, we consider three α values (hence three SSP families): The derived [α/Fe] and its corresponding upper and lower errors, as reported in Table 2. In Fig. 2, we show an example of the fit performed by STARLIGHT over the integrated spectrum of VCC2019 (the dark blue spectrum) using three SSP families with [α/Fe] = [0.22, 0.26, 0.30] dex. The best-fitted solution of STARLIGHT (shown in red) and the fit residuals (shown in light purple) are also plotted in this figure. Please note that the residuals are shifted up by 0.3 for displaying purposes.

To account for possible systematic errors, we first perform a single fit over the integrated spectrum of each dE. By randomly selecting a value from the residuals of this initial fit and adding that to the original flux, at each wavelength, we create 100 perturbed spectra and repeat the fitting on each of them. The results of our procedure are discussed in Section 4.3.

4 RESULTS

4.1 Integrated stellar properties

As summarized in Table 2, our dEs span the age range of 2.10–10.50 Gyr, the metallicity range $-0.77 <$ [M/H] [dex] < -0.37 and the [α/Fe] interval between 0.14 and 0.43 dex. The youngest stellar populations, with an average age = 2.10 Gyr and a mean [M/H] = -0.61 dex, are detected in VCC0170, while the oldest stellar populations are observed in VCC1896 and VCC2019. VCC1836 is the most metal-poor dE in our sample with [M/H] = -0.77 dex, while VCC1833 the most metal-rich with [M/H] = -0.37 dex. Additionally, VCC0794 is the most α-enhanced member of our sample with [α/Fe] = 0.43 dex. Given the stellar mass range of our sample, we find our derived [M/H] values for this sample to be in good agreement with the general mass−metallicity scaling relation (e.g. Gallazzi et al. 2005; Panter et al. 2008; González Delgado et al. 2014; Sybilska et al. 2017).

VCC0170, VCC0794, and VCC0990 have been investigated as part of the SMAKCED project by Toloba et al. (2014). We find our measurements for VCC0170 and VCC0794 to be in good agreement with their results. In detail, Toloba et al. (2014) reported a light-weighted age of 2.0 ± 0.4 Gyr (compared to 2.10 ± 0.20 in this study) and [M/H] of -0.50 ± 0.10 dex (compared to -0.61 ± 0.04 dex derived here) for VCC0170. Similarly, they reported a light-weighted age of 7.8 ± 1.8 Gyr (compared to 9.90 ± 0.40 in this study) and [M/H] of -0.8 ± 0.1 dex (compared to -0.73 ± 0.02 dex obtained here) for VCC0794. However, we estimate an older age for VCC0990 ($7.77^{+3.59}_{-1.59}$ Gyr) than what was determined by Toloba et al. (2014) (4.0 ± 1.2 Gyr). Nevertheless, this discrepancy is less than 2σ and not significant.

In Fig. 3, we compare the stellar population parameters of our sample of dEs with those of our comparison samples (see Section 2). On the top row and from left to right, we present the age, [M/H],[3] and [α/Fe] distributions of the Coma dEs (in grey), the Virgo dEs (in pink) and our sample of dEs (in brown). In terms of light-weighted age distribution, our dEs are not significantly different from other dwarf ellipticals in the Virgo and Coma clusters. The middle upper panel of Fig. 3 shows that, despite their similarities in age, Virgo dEs (including our dEs) are more metal-poor than their counterparts in the Coma cluster (with a median [M/H] of -0.36 ± 0.02 dex and -0.59 ± 0.04 dex for the Coma and Virgo clusters, respectively). This can be either due to the lower number of investigated Virgo dEs within the given stellar mass range or the different characteristics of these two clusters (particularly their dynamical stage and halo size). Nonetheless, investigating the different characteristics of these two massive galaxy clusters is beyond the scope of this paper.

Note that, remarkably, the distribution of [α/Fe] in the right-hand panel indicates that our dEs are more α-enhanced (with a median [α/Fe] = 0.26 ± 0.02 dex) than those in the Virgo and Coma clusters (with a median [α/Fe] of 0.05 ± 0.03 dex and 0.10 ± 0.01 dex, respectively).

The projected phase-space diagram of a cluster, which combines cluster-centric velocity with cluster-centric radius, allows us to estimate an average infall time for the cluster's galaxies, and hence how long they have been exposed to the cluster's environmental effects (Rhee et al. 2017; Pasquali et al. 2019; Smith et al. 2019). To check for a possible correlation between the stellar population properties of dEs and their infall time, we present the projected phase-space distribution of our sample along with the Virgo and Coma comparison samples in the bottom row of Fig. 3. In each panel and from left to right, the data points are colour coded based on their age, [M/H] and [α/Fe]. Different symbols indicate members of different clusters. In each panel, three different zones are marked, indicating different average infall times ($\overline{T}_{inf}$), obtained from Pasquali et al. (2019) and Smith et al. (2019). In this regard, our zone 3 corresponds to $\overline{T}_{inf} > 5$ Gyr, zone 2 indicates $5 < \overline{T}_{inf} < 3$ Gyr and zone 1 indicates $\overline{T}_{inf} < 3$ Gyr. Our dEs are denoted with coloured squares and are marked with a solid-line rectangle. Detailed information on the statistics of each zone is presented in Table 3 and is also discussed below.

Median age – According to this table, the median age of all dEs in zone 3 is 7.4 ± 0.5 Gyr, and in zone 2, after excluding our sample of dEs, 7.77 ± 0.5 Gyr. Our dEs with a median age of 6.8 ± 1.1 Gyr are consistent with the dEs in both zone 2 and 3 (within the 1σ level). However, despite their similar stellar mass and average infall time, they show a remarkable scatter in their ages, which might be related to pre-processing in their previous host group. We elaborate more on this in Section 5.1.

Median metallicity – The median light-weighted [M/H] of all cluster dEs shows no trend with their average infall time. All dEs in zone 3 have a median [M/H] = -0.40 ± 0.05 dex, and -0.40 ± 0.03 dex in zone 2. Our dEs are more metal-poor than the dEs of zone 2 and 3, with a median [M/H] = -0.59 ± 0.05 dex (within the 2σ level). More specifically in zone 2, our dEs are more metal-rich than Virgo dEs (with median [M/H] = -0.62 ± 0.06), but metal-poorer than Coma dEs (with median [M/H] = -0.36 ± 0.05). It should be noted, however, that the statistics presented for the Virgo dEs are possibly affected by the small number of data points available for this cluster.

Median [α/Fe] – The median [α/Fe] value of the cluster dEs, excluding our sample of dEs, is ∼0.10 dex in both zones 2 and 3, and does not show any evident correlation with the average infall time. Our dEs have a median value of 0.26 ± 0.02 dex, thus are more α-enhanced than the Coma and Virgo comparison samples, at any given infall time. Additionally, our dEs fall within a narrow range of

[3]To convert the [Fe/H] values reported in Smith et al. (2009) to [M/H], which we use in this study, the conversion of [M/H] ∼ [Fe/H] + log(0.694f$_\alpha$ + 0.306), is performed where $f_\alpha = 10^{[\alpha/Fe]}$ (Salaris & Cassisi 2005)

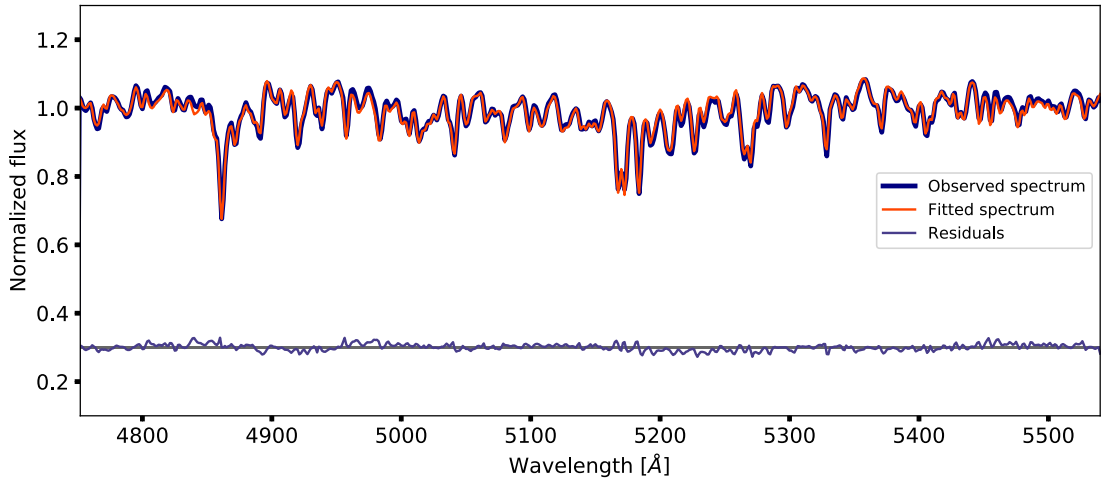

Figure 2. An example of the full spectrum fitting over the averaged spectrum of VCC2019. The observed and normalized spectrum is plotted in dark blue. STARLIGHT best-fitting synthetic spectrum is shown in red, and the residuals of the fit are shown in light purple. For better legibility, the residuals are shifted up by 0.3.

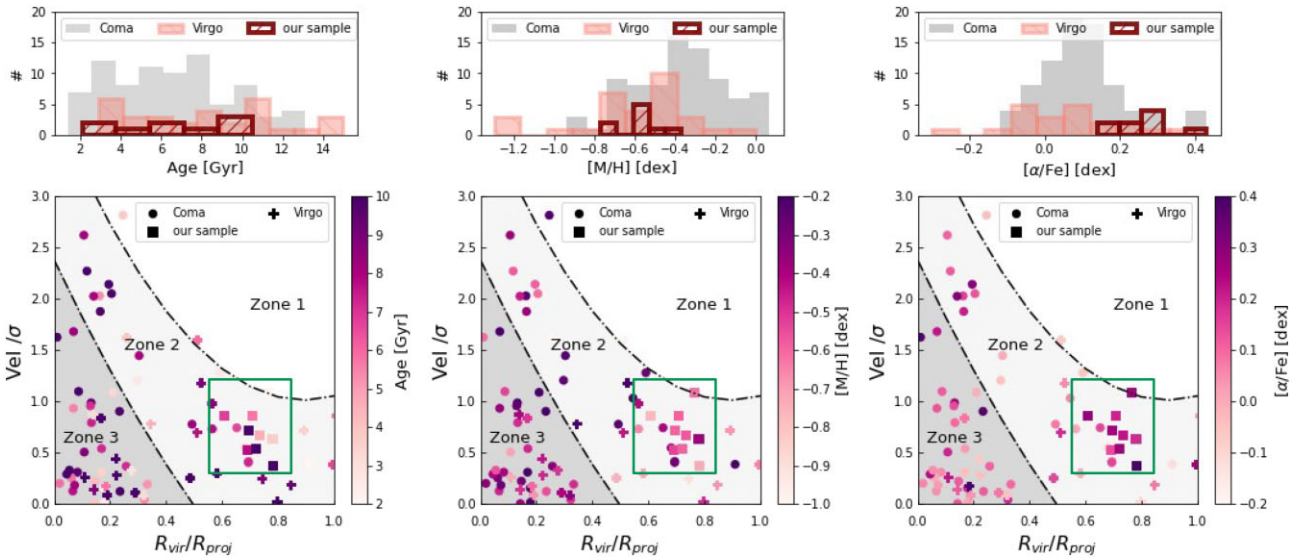

Figure 3. *Top row*: From left to right, the age, [M/H], and [α/Fe] distributions of the Coma dEs (in grey), the Virgo dEs (in pink) and our sample of dEs (in brown) are presented. All dEs have $-17 \geq M_r$ [mag] > -18. *Bottom row*: From left to right, the projected phase-space distributions of the Virgo dEs (denoted with a plus symbol), Coma dEs (denoted with circle) and our sample of dEs (denoted with squares) colour coded for age, [M/H] and [α/Fe] in each panel, respectively. Our dEs are further marked with a green solid-line rectangle. Different zones of the projected phase-space diagram indicate different average infall times ($\overline{T}_{inf}$) to the host halo, obtained from Pasquali et al. (2019) and Smith et al. (2019). In detail: zone 1: $\overline{T}_{inf} < 3$ Gyr; zone 2: 3 Gyr $< \overline{T}_{inf} < 5$ Gyr; zone 3: $\overline{T}_{inf} > 5$ Gyr.

$0.14 <$ [α/Fe] [dex] < 0.43. These values are comparable with what is reported for giant early-type galaxies (e.g. Gallazzi et al. 2006; La Barbera et al. 2014; Gallazzi et al. 2021) and thick-disc stars of the Milky Way (e.g. Bensby, Feltzing & Lundström 2003; Vincenzo et al. 2021).

4.2 On the [α/Fe] ratio of our sample dEs

Despite having a similar stellar mass, our dEs show larger [α/Fe] values compared to their counterparts in the Coma and Virgo clusters. One possible reason for this difference can be the use of different Fe absorption lines to estimate the [α/Fe] ratio. We estimate [α/Fe] through the combination of the Mgb, Fe5270, and Fe5335 Lick indices, similarly to Smith et al. (2009) in their analysis for dEs in Coma. However, the [α/Fe] ratios derived by Sybilska et al. (2017) are based only on the Mgb and Fe5015 indices.

We therefore repeat our measurements using the same indices as in Sybilska et al. (2017). To be consistent with their method, we derive age, [M/H], and [α/Fe] only by going through the first two Steps described in Section 3.3, and by using only the H β_0, Mgb, and Fe5015 indices. We apply this approach to our sample of dEs and Sybilska et al. (2017) sample. A one-to-one comparison of the derived [M/H] and [α/Fe] values in this test with the original measurements is presented in the top and bottom panels of Fig. 4, respectively.

Table 3. Median stellar population properties of our sample of dEs and the comparison samples in each infall zone.

Cluster	Median of	Zone 3	Zone 2
Coma	Age (Gyr)	7.2 ± 0.54	7.55 ± 0.7
	[M/H] (dex)	-0.36 ± 0.03	-0.31 ± 0.04
	[α/Fe] (dex)	0.12 ± 0.02	0.09 ± 0.03
Virgo	Age (Gyr)	9.57 ± 1.07	8.22 ± 0.8
	[M/H] (dex)	-0.49 ± 0.03	-0.62 ± 0.06
	[α/Fe] (dex)	0.08 ± 0.04	0.05 ± 0.03
Our sample	Age (Gyr)	—	6.8 ± 1.1
	[M/H] (dex)	—	-0.59 ± 0.05
	[α/Fe] (dex)	—	0.26 ± 0.02
All data points[a]	Age (Gyr)	7.40 ± 0.5	7.77 ± 0.5
	[M/H] (dex)	-0.40 ± 0.05	-0.40 ± 0.03
	[α/Fe] (dex)	0.10 ± 0.02	0.08 ± 0.02

Notes. The columns show: Name of the cluster, stellar population property for which we are reporting median values, median values in zone 3, and median values in zone 2.
[a]Computed after excluding our sample of dEs.

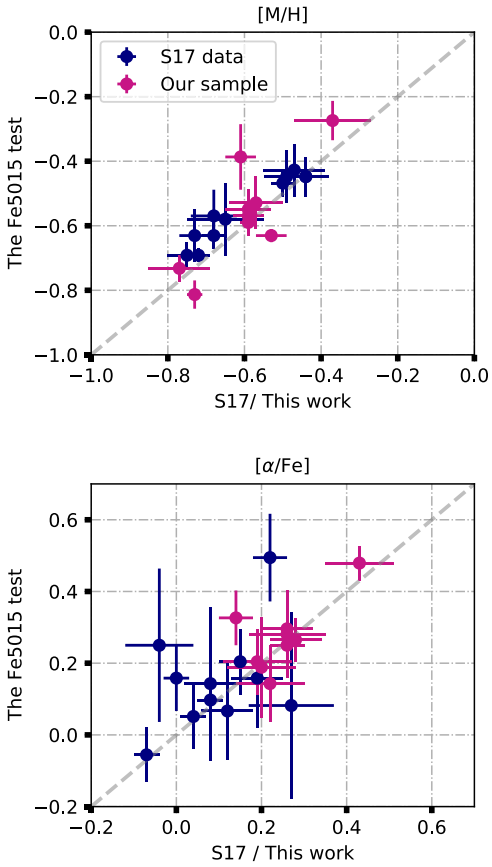

Figure 4. Metallicities and [α/Fe] ratios obtained from Steps 1 and 2 of our method, relying on the Fe5015 index, are shown on the y-axis of the top and bottom panels, respectively. On the x-axis of each panel, we compare the Fe5015 test results with the original estimates of Sybilska et al. (2017) (S17, blue data points) and the values of Table 2 for our sample of dEs (pink data points). Error bars are computed in the same way as described in Section 3.

On the y-axis of each panel in Fig. 4, we show the [M/H] ([α/Fe]) values obtained only from Steps 1 and 2 of our method, relying on the Fe5015 index, for both our sample of dEs and Sybilska et al. (2017) sample. This set of values is labelled as 'The Fe5015 test'. On the x-axis, we compare 'The Fe5015 test' results with the original measurements of Sybilska et al. (2017) (S17, shown with blue data points). Pink data points show the comparison between 'The Fe5015 test' results and our original estimates for our sample of dEs (obtained from Table 2). We find that, despite changing Lick index pairs in our fitting procedure, our dEs still show a distinct [α/Fe] distribution, albeit with a slightly different range of values. Specifically, by fitting only over the Fe5015 absorption line, our sample of dEs falls within the range of $0.18 <$ [α/Fe] [dex] < 0.49, instead of $0.14 <$ [α/Fe] [dex] < 0.43 as obtained with our original method.

This comparison shows that choosing different Fe absorption features has negligible effects on the derived [α/Fe] values of our dEs. Hence, the distinct [α/Fe] distribution of our sample dEs, compared with Sybilska et al. (2017)'s sample, is not due to systematics. We compare the [α/Fe] values of our sample of dEs (derived in this section) with those of Sybilska et al. (2017), using the K–S and the Anderson–Darling tests. Both tests indicate that the difference between the [α/Fe] distributions of the two samples is significant (with p-values $= 0.03$ and 0.009, respectively).

4.3 Star formation histories of our sample dEs

As explained in Section 3.4, we perform the full spectrum fitting using STARLIGHT, for 100 MC realizations over each dE's averaged spectrum. We derive light-weighted values of age and [M/H] from each MC run, following the definitions below:

$$< \text{Age} >_{\text{L}} = \sum_{t,Z|\alpha} \epsilon_{t,Z|\alpha} \text{Age} \tag{3}$$

$$< [\text{M/H}] >_{\text{L}} = \sum_{t,Z|\alpha} \epsilon_{t,Z|\alpha} [\text{M/H}], \tag{4}$$

where t, Z, and α denote age, metallicity and [α/Fe] ratio of a given SSP model, respectively, and $\epsilon_{t,Z|\alpha}$ is the light-weighted stellar population vector. The latter indicates the flux contribution of each SSP model to the best-fitting spectrum. Here the summation is over the entire base models, at fixed α. To compute the mass-weighted age and metallicity, we use the same equations but with $\mu_{t,Z|\alpha}$, which is the mass-weighted stellar population vector. This vector is computed through multiplying $\epsilon_{t,Z|\alpha}$ by the mass-to-light ratio of each SSP

(computed by STARLIGHT for each fit). In Table 4, we report the light- and mass-weighted ages and metallicities averaged over the results of the 100 MC runs. Their upper and lower errors are the 84th and 16th percentiles of their corresponding distributions. In Appendix B, we compare the values of light-weighted age and [M/H] that were obtained through full spectrum fitting with those derived by our method described in Section 3.3. The comparison shows that the differences in age and [M/H] results between our index fitting method and STARLIGHT are typically significant at a 2σ level. STARLIGHT reports, on average, younger ages and higher [M/H]. The largest discrepancy concerns the age of VCC2019, for which STARLIGHT estimates a value of 6.5 Gyr (compared to ∼10.5 Gyr from our index fitting method). In Appendix C, we show that the presence of a young nuclear star cluster in the core of VCC2019 leverages the contribution of younger SSPs in the STARLIGHT final best fit for this dE. The central nuclear star cluster hosts a distinct, younger stellar population compared to the rest of VCC2019 and noticeably contributes to its integrated light (see Paudel et al. 2010; Fahrion et al. 2021).

In the top row of Fig. 5, we present the stellar light fraction ($\epsilon_{t,\,Z|\alpha}$) as a function of look-back time for each dE in our sample. Each distribution is constructed by summing $\epsilon_{t,\,Z|\alpha}$ of the base models of the same age but different metallicity and [α/Fe] ratio. These light distributions are sensitive to the contribution of young stars to the total observed light. Thus, they trace the more recently formed stars in a given dE. Here we divide galaxies into two sub-samples based on the presence or absence of a peak in their light fraction profiles at ∼2–3 Gyr. In the lower panels of this figure, we present the stellar mass fraction ($\mu_{t,\,Z|\alpha}$) as a function of look-back time, which is constructed by summing $\mu_{t,\,Z|\alpha}$ of the base models of the same age but different metallicity and [α/Fe]. For each dE, the mass-weighted distribution follows a similar trend as the light-weighted one. In all four panels of Fig. 5, two dashed vertical lines indicate two estimates for the average infall time ($\overline{T}_{\rm inf}$) of our sample dEs, based on the results of Lisker et al. (2018) (the red line) and Pasquali et al. (2019) (the black line).

The six dEs in the left-hand panels of Fig. 5 seem to have experienced a rather prolonged star formation activity at low rate, which has later undergone a sudden boost during or after their accretion on to Virgo. On the contrary, two of the dEs in the right-hand panels of Fig. 5 (namely VCC0794 and VCC1896) exhibit a shorter star formation activity that culminated about 8–10 Gyr ago. VCC2019 also follows a similar trend, after excluding its central nuclear star cluster from its integrated spectrum (see Appendix C).

In the top panel of Fig. 6, we plot the cumulative mass fraction of these six dEs as a function of look-back time. Our results indicate that this sub-population has experienced distinguishable, yet diverse (ranging from 5 to more than 70 per cent), mass growth since the accretion event (i.e. between 4 and 1 Gyr ago). According to Fig. 6 VCC0170, where B20 detected ongoing star formation, has experienced the most drastic mass growth (∼70 per cent) since ∼4 Gyr ago. Our results for these six dEs are in general agreement with the 'delayed-then-rapid' quenching scenario of Wetzel et al. (2013) (see Section 5), in which galaxies are predicted to grow in mass by up to 50 per cent after their accretion on to clusters. Regarding the remaining three dEs in our sample, their distributions of cumulative mass fraction in Fig. 6 indicate that they formed their current total stellar mass more than 4 Gyr ago, before their accretion on to Virgo and possibly in their previous host group.

In Section 4.1, we show that VCC0794 is the most α-enhanced member of our sample. The spectral indices of this dE point to old (∼10 Gyr) and metal-poor (∼−0.73 dex) stellar populations (Table 2). In the top right panel of Fig. 5, this particular dE shows a peak in its stellar light fraction profile at the age of 9 Gyr, which is consistent with our previous results and endorses the fact that this dE has been accreted on to Virgo already old and quenched. The profile of this particular dE indicates that the bulk of its stellar population formed in a rather short time interval (∼4 Gyr), which can explain its high value of [α/Fe].

Two dEs of our sample, namely VCC0990 and VCC2019, show double peaks in their stellar light and mass fraction profiles. According to our results in Appendix C, the peak at younger ages (i.e. at ∼2 Gyr for VCC0990 and ∼4 Gyr for VCC2019) is mostly due to their nuclear star cluster, while the second peak at older ages appears to be related to star formation in their main body. We note that the exclusion of the nuclear star cluster from the galaxy's integrated spectrum (Fig. C1) significantly reduces the amplitude of the peak at younger ages in the star formation history of both galaxies. It thus appears that VCC2019 was accreted on to Virgo with its main body already pre-processed and quenched (also in Fahrion et al. 2021). A detailed investigation on the spatial distribution of stellar population properties of these two dEs (along with the rest of our sample) will be presented in a forthcoming paper.

Our results, constructed from 100 MC iterations, present only 100 possible fitting solutions for the spectral energy distribution of each dE. In order to have a realistic interpretation of these results, however, we need to also take inevitable sources of uncertainty into account. Our full spectrum fitting, performed with STARLIGHT, is based on a limited number of SSP models, which may not be enough to break the well-known 'age–metallicity degeneracy', especially for ages older than 1 Gyr (Shen & Yin 2020). Yet, Sánchez-Blázquez et al. (2011) showed that the age–metallicity degeneracy is less prominent in the full spectrum fitting technique compared to the Lick indices method. This degeneracy may affect the accurate age dating of the stellar light fraction peaks in Fig. 5 (possibly shifting them by 1 to 2 Gyr), but given the uncertainties in the accretion time of our sample dEs, we believe that this does not significantly affect our results and conclusions.

5 DISCUSSION

Due to their shallow potential well, low-mass galaxies are quite susceptible to environmental processes, such as ram pressure stripping (Gunn & Gott 1972), strangulation (Larson et al. 1980), and harassment (Moore et al. 1996, 1998), which can alter their morphology, star formation activity, and kinematics on different time-scales (e.g. Boselli & Gavazzi 2006; Boselli et al. 2021). For instance, low-mass satellites grow older and metal-richer as the mass of their host haloes increases, whilst their star formation rate declines and their [α/Fe] abundance ratio remains unchanged (Pasquali et al. 2010, 2019; Coenda et al. 2020; Tiwari, Mahajan & Singh 2020; Gallazzi et al. 2021; Trussler et al. 2021). In the projected phase-space diagram, cluster low-mass galaxies with larger infall time (i.e. longer exposures to the cluster environment) are observed to be dominated by older, metal-richer and more [α/Fe] enhanced stellar populations, compared to their recently accreted counterparts (Pasquali et al. 2019; Gallazzi et al. 2021).

The aforementioned trends are mainly explained within the so-called 'delayed-then-rapid' scenario (e.g. Wetzel et al. 2013; Wheeler et al. 2014; Oman & Hudson 2016; Maier et al. 2019a, b; Rhee et al. 2020). In this context, the star formation rate of newly accreted low-mass galaxies remains unaffected for several Gyr after their first infall. During this 'delayed phase', low-mass star-forming galaxies

Table 4. Integrated light-/mass-weighted stellar population properties of our sample dEs as derived by STARLIGHT.

Object	M_B (mag)	$<Age>_L$ (Gyr)	$<[M/H]>_L$ (dex)	$<Age>_M$ (Gyr)	$<[M/H]>_M$ (dex)
VCC0170	−16.63	$2.09^{+0.20}_{-0.24}$	$-0.54^{+0.04}_{-0.04}$	$2.78^{+0.21}_{-0.19}$	$-0.61^{+0.12}_{-0.10}$
VCC0407	−16.38	$4.11^{+0.35}_{-0.42}$	$-0.50^{+0.03}_{-0.03}$	$4.70^{+0.31}_{-0.34}$	$-0.56^{+0.13}_{-0.11}$
VCC0608	−16.59	$3.16^{+0.27}_{-0.66}$	$-0.44^{+0.04}_{-0.04}$	$4.58^{+0.20}_{-0.34}$	$-0.48^{+0.14}_{-0.11}$
VCC0794	−16.30	$9.54^{+0.58}_{-0.52}$	$-0.69^{+0.05}_{-0.05}$	$9.91^{+0.83}_{-0.78}$	$-0.62^{+0.14}_{-0.10}$
VCC0990	−16.44	$4.37^{+0.43}_{-0.50}$	$-0.38^{+0.04}_{-0.04}$	$5.30^{+0.40}_{-0.38}$	$-0.37^{+0.09}_{-0.11}$
VCC1833	−16.45	$5.16^{+0.20}_{-0.82}$	$-0.28^{+0.08}_{-0.08}$	$7.17^{+0.36}_{-0.25}$	$-0.27^{+0.09}_{-0.09}$
VCC1836	−16.46	$3.98^{+0.45}_{-0.38}$	$-0.66^{+0.05}_{-0.05}$	$4.56^{+0.33}_{-0.28}$	$-0.72^{+0.20}_{-0.16}$
VCC1896	−16.05	$8.60^{+0.43}_{-0.57}$	$-0.49^{+0.04}_{-0.03}$	$9.06^{+0.76}_{-0.70}$	$-0.43^{+0.18}_{-0.10}$
VCC2019	−16.66	$6.51^{+0.60}_{-0.65}$	$-0.46^{+0.05}_{-0.04}$	$6.81^{+0.49}_{-0.41}$	$-0.45^{+0.12}_{-0.08}$

Note. The columns show: name of the target, total *R*-band magnitude, light-weighted age, light-weighted metallicity, mass-weighted age, and mass-weighted metallicity. M_B is derived from the observed M_r using the *B*–*r* colour computed by MILES SSPs with the same age and metallicity as estimated for each dE.

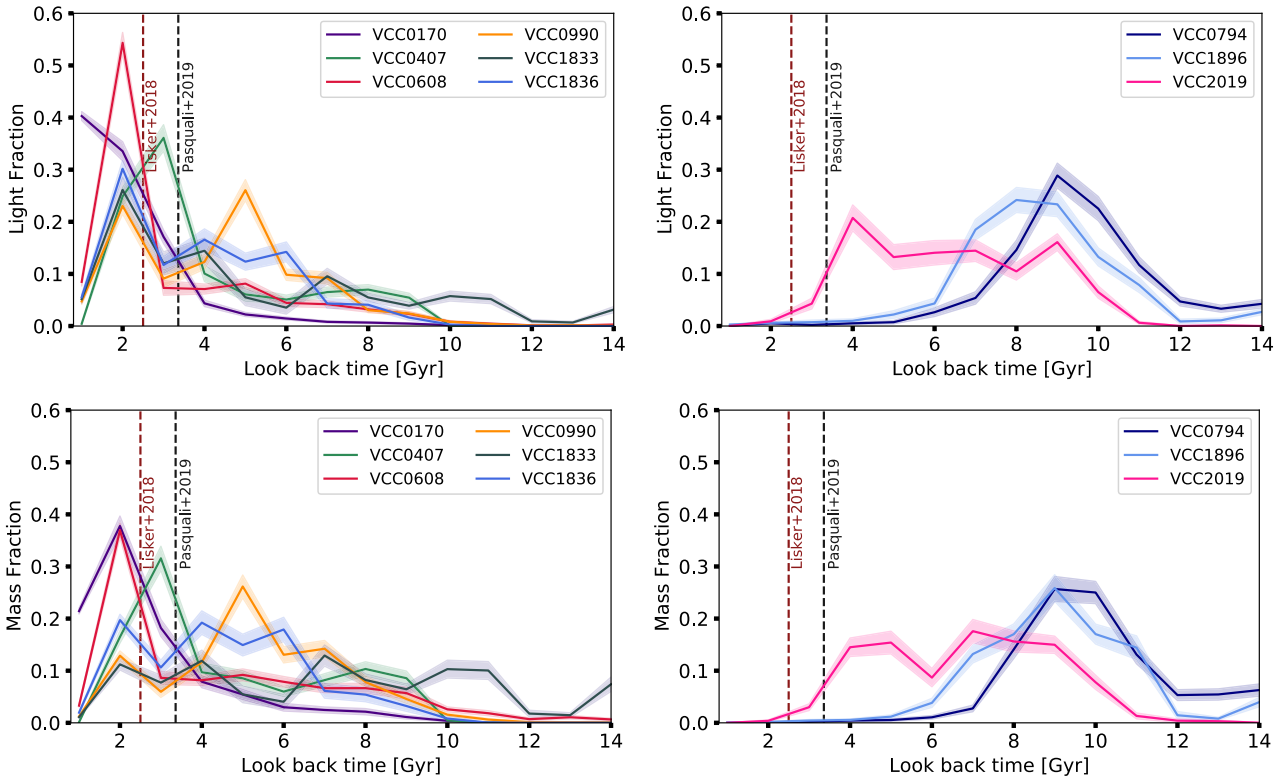

Figure 5. *Top row:* The stellar light fraction ($\epsilon_{t,\,Z|\alpha}$) of our sample of dEs as a function of time. The profiles of those dEs that exhibit a prominent peak after their accretion on to the Virgo cluster are presented in the left-hand panel, and the distributions of those dEs without a similar peak are shown in the right-hand panel. *Bottom row:* Same as the top row but for the mass weighted fractions ($\mu_{t,\,Z|\alpha}$). The red and black dashed vertical lines indicate the accretion time of our sampled dEs on to Virgo as predicted by Lisker et al. (2018) and Pasquali et al. (2019), respectively.

are predicted to experience noticeable (up to 50 per cent) mass growth (Wetzel et al. 2013). During the subsequent 'rapid phase' they are predicted to reduce their star formation rate with an e-folding time of <0.8 Gyr (Wetzel et al. 2013; Rhee et al. 2020). The rapid phase is possibly driven by ram pressure stripping, which is more efficient in the central regions of massive galaxy groups and clusters. Furthermore, ram pressure can compress the gas in the inner galaxy disc (e.g. Boselli et al. 2021) and, therefore, trigger a new episode of star formation or enhance a pre-existing one (Fujita 1998; Fujita & Nagashima 1999; Vollmer et al. 2001). It should be noted that the quenching time-scales predicted by this scenario are independent of host halo mass, and they cannot reproduce the observed increase of the quiescent fraction of low-mass galaxies with halo mass. The scenario thus requires that up to 50 per cent of the quenched low-mass

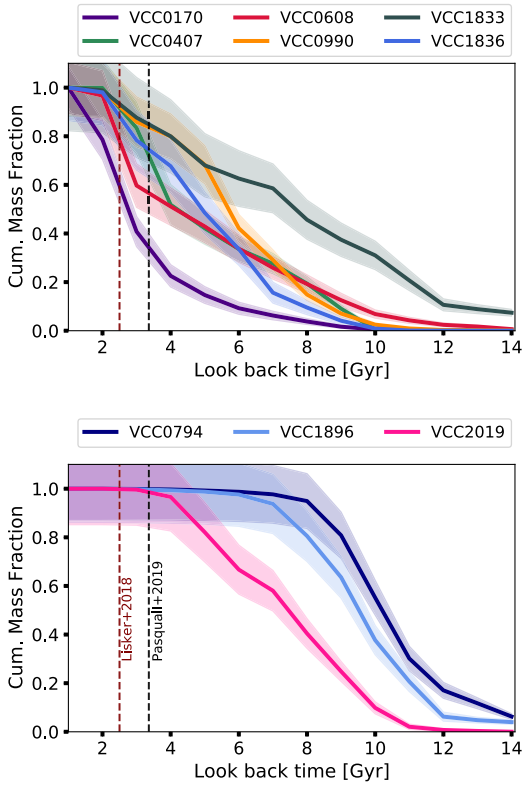

Figure 6. The cumulative mass distribution as a function of look back time (in Gyr) plotted for our sample dEs with (top panel) and without (bottom panel) a recent episode of star formation. Here, galaxies are divided into two sub-samples following Fig. 5. The red and black dashed vertical lines indicate the accretion time of our sample of dEs on to Virgo as estimated by Lisker et al. (2018) and Pasquali et al. (2019), respectively.

galaxies in present-day host haloes to be accreted already quenched prior infall, presumably in lower mass haloes.

In what follows, we use the stellar population properties and star formation histories of our sample of dEs to discuss their pre-processing within their previous group environment and their on-going processing within Virgo, their present-day host halo.

5.1 The high [α/Fe] ratio of dEs and their infall time

The [α/Fe] abundance ratio is typically interpreted as an indicator of the duration of star formation in a given galaxy prior to the onset of significant contributions from SNe of Type Ia, in the sense that rapid or early quenching of star formation, can result in a higher [α/Fe] ratio (e.g. Balogh et al. 1998; Thomas, Greggio & Bender 1999; de La Rosa et al. 2011; Santos et al. 2015). Since dEs are more prone to environmental effects, one can expect a correlation between their chemical abundance ratio and their host environment. Yet, results in this regard seem contradictory. For instance, Michielsen et al. (2008) did not detect any correlation between the [α/Fe] ratios and local density of very bright Virgo dEs (i.e. $M_r < -15.5$ mag) (see also Thomas et al. 2005; Paudel et al. 2010). On the other hand, Smith et al. (2009) showed that the [α/Fe] ratio of dEs in the Coma cluster decreases towards larger cluster-centric distances, from [α/Fe] $\sim$ 0.15 dex in the cluster centre to [α/Fe] $\sim$ 0.0 dex in the cluster outskirts. A similar trend was also observed for Virgo dEs (Liu et al. 2016) and low-mass galaxies in Abell 496 (Chilingarian et al. 2008), albeit with high uncertainty (see also Penny & Conselice 2008).

We note that the [α/Fe] ratios obtained here for our sample of dEs contrast with the findings mentioned above as well as with the [α/Fe]–$\overline{T}_{inf}$ correlation found by Pasquali et al. (2019) (see also Gallazzi et al. 2021). In spite of their large cluster-centric distance ($\sim$1.5 Mpc from M87) and small $\overline{T}_{inf}$, our dEs show high (not low) [α/Fe] ratios (i.e. $>$ 0.2 dex), which are more similar to those of ancient infallers (with $\overline{T}_{inf} > 5$ Gyr Pasquali et al. (2019)) or even to those of massive ETGs (e.g. Gallazzi et al. 2006; La Barbera et al. 2014; Gallazzi et al. 2021). We find our sample of dEs to be more α-enhanced (at a 8σ level) than their counterparts in the Virgo and Coma clusters, at similar or even larger $\overline{T}_{inf}$. Moreover, our dEs are α-enhanced irrespectively of their luminosity-weighted ages. Such high [α/Fe] ratios might be explained if our dEs had been affected by environmental processes not only during, but also before their accretion on to Virgo. We elaborate more on this in Section 5.2.

5.2 Pre-processing in the group versus early processing in Virgo

As shown by the star-formation histories (SFHs) of our sample of dEs (Section 4.3), six of these galaxies have undergone a recent phase of star formation, during or right after their accretion on to the Virgo cluster (hereafter, rSF-dEs), while the remaining three dEs show no signs of 'recent' star formation, having ceased to form stars long before their accretion on to Virgo (hereafter, pSF-dEs).

The high [α/Fe] of rSF- and pSF-dEs could be explained as follows:

rSF-dEs. These galaxies experienced distinguishable, yet diverse (ranging from 5 to more than 70 per cent), mass growth within a short period of time during/after the accretion event (i.e. between 4 and 1 Gyr ago). The short duration of recent star formation in the rSF-dEs is also consistent with these galaxies having similar (not higher) metallicities than the rest of our sample. Hence, at least some of the rSF-dEs could have high light-weighted [α/Fe], because of the short star formation event that they experienced after accretion on to Virgo.

*pSF-dEs.*These galaxies do not show any peak in their recent SFH, and completed the formation of their present-day stellar mass more than 4 Gyr ago (see right-hand panel of Fig. 5). In particular, VCC0794 formed most of its stellar mass $\sim$5 Gyr before accretion on to Virgo, within a time-scale of $\sim$2 Gyr,[4] in agreement with its high [α/Fe] ($\sim$0.43 dex) and low metallicity ($\sim-$0.73 dex; see Table 2). We thus suggest that the high [α/Fe] ratio of the pSF-dEs might be the result of pre-processing in their host group prior infall into Virgo.

However, as the sub-samples of rSF- and pSF-dEs exhibit very similar metallicities and [α/Fe] ratios (see Table 2), their [α/Fe] values might have a common origin. Indeed, metallic lines are far shallower in young, relative to old, stellar populations (Walcher et al. 2009; Conroy 2013), and therefore our [M/H] and [α/Fe] estimates might be reflecting, for all galaxies, the properties of the old component, which was pre-processed in their host group prior accretion on to Virgo, as discussed above for the sample of pSF-dEs. In order to distinguish between the two scenarios (early effect of Virgo versus pre-processing in the previous host group) one would need to derive the chemical enrichment history of our sample dEs which, however, requires a larger spectral range (more extended to the blue) than provided by MUSE.

[4]This can be roughly estimated, by eye, as the time since the star formation ceased after its peak value.

Regarding the origin of the recent star formation undergone by the rSF-dEs, we speculate that the ram pressure exerted by the Virgo intracluster medium on these galaxies might be responsible for it. In fact, by compressing the cold gas in the inner disc of galaxies during their early accretion, ram pressure can increase the central gas surface density by up to a factor of 1.5, and lead to a temporary enhancement of the star formation rate by up to a factor of 2 in the central regions of the infalling galaxies (Vollmer et al. 2001; Steyrleithner, Hensler & Boselli 2020). The presence of nebular emission lines powered by ongoing star formation in the spectra of VCC0170 might be a signpost of such an effect. On the other hand, the non-detection of ionized gas in the MUSE spectra of the remaining rSF-dEs might indicate that these galaxies had a lower gas reservoirs at infall, and/or consumed it faster. An alternative to our interpretation is that these recent episodes of star formation might be the result of the intrinsic star formation activity of these galaxies.

Since we interpret the high [α/Fe] of the pSF-dEs in our sample as an indication of their pre-processed nature, the smaller [α/Fe] values of the Virgo and Coma comparison samples in Fig. 3 may suggest that pre-processing is not that important for the overall population of cluster dEs, despite predictions of a significantly large fraction of pre-processed galaxies in clusters (e.g. McGee et al. 2009; Wetzel et al. 2013). However, the level of pre-processing depends on the gas content of a galaxy, the mass of its previous host halo as well as on its infall time on to such halo. Hence, determining the number of dEs with similar level of pre-processing as in our sample is very challenging, and is hampered by the limited size of our comparison samples, particularly in the Virgo cluster. Based on our results, one should not conclude that pre-processing is a rare condition in present-day clusters. We also note that the high [α/Fe] of the rSF-dEs in our sample is likely due to a rather short and recent phase of star formation, taking place less than $\sim$4 Gyr ago. It is thus a recent event that cannot be traced in dEs with larger $\overline{T}_{inf}$ (i.e. zone 3) or those pre-processed recent infallers that are already gas deficient before their accretion on to the cluster (i.e. zone 2 and 1).

5.3 Linking kinematics and stellar age of dEs

In B20, we showed that the specific angular momentum (λ_R) profiles of our sample of dEs vary between those of low-mass, star-forming galaxies in the field and those of equally massive Virgo dEs with larger infall times. We interpreted the scatter in λ_R among our sample of dEs as possibly due to pre-processing in their host group prior to infall into Virgo, since the Virgo cluster can modify the kinematics of its satellites only after several pericenter passages (i.e. several Gyr, Boselli & Gavazzi 2006), while our dEs were accreted less than 3 Gyr ago.

In Fig. 7, we plot λ_{Re}, the specific angular momentum measured at $1R_e$, as a function of mean light-weighted age (within $1R_e$) for Virgo dEs (in dark blue, Ryś et al. 2014; Sybilska et al. 2017) and low-mass, late-type galaxies in the field from the CALIFA survey (in light blue, Falcón-Barroso et al. 2019; González Delgado et al. 2015). A detailed description of the field comparison sample is presented in B20. Here we note that the light-weighted ages of the Virgo dEs sample were derived using the Lick indices, while the light-weighted ages of the CALIFA sample were obtained using the full spectrum fitting technique with STARLIGHT. For our sample we use the light-weighted ages computed with our Lick indices fitting routine. The Virgo dEs shown in this plot have larger infall times ($\overline{T}_{inf} > 3$ Gyr) than our sample of dEs, while the CALIFA late-type galaxies can be considered to have $\overline{T}_{inf} = 0$.

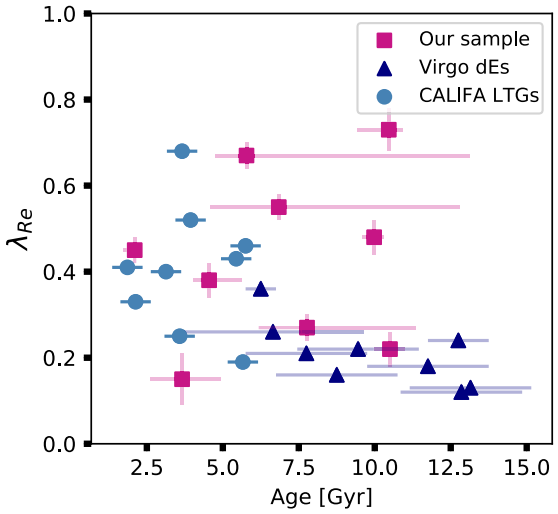

Figure 7. This plot shows the specific angular momentum at $1R_e$ (λ_{Re}) versus mean light-weighted age within $1R_e$ of our sample of dEs and two comparison samples. Light blue circles indicate low-mass late-type field galaxies selected from the CALIFA sample. The λ_{Re} and age values are taken from Falcón-Barroso et al. (2019) and González Delgado et al. (2015), respectively. Dark blue triangles denote Virgo dEs with $\overline{T}_{inf} > 3$ Gyr. The λ_{Re} and age values for this sample are taken from Ryś et al. (2014) and Sybilska et al. (2017), respectively. Pink squares indicate members of the nine dEs investigated in this study. The λ_{Re} and age values are taken from B20 and Table 2, respectively.

We see that these two comparison samples define a trend of decreasing λ_{Re} with increasing light-weighted age. As star formation gradually fades due to gas consumption and/or gas loss triggered by the environment, galaxy kinematics progressively changes from being dominated by rotation to being pressure supported. The λ_{Re}–age relation of Fig. 7 is consistent with that derived by Falcón-Barroso et al. (2019) over a larger stellar mass range, and is also predicted by semi-analytical models of galaxy formation and evolution, according to which gas-rich galaxies (with $M_\star/\,M_\odot > 10^9$) have larger λ_{Re} (Zoldan et al. 2018).

Our dEs (denoted with pink squares) generally follow the relation defined by our two comparison samples, except for two galaxies that are several σ away from it, being too old ($\sim$ 10 Gyr) for their high λ_{Re}.

Under the assumption that their accretion on to Virgo is too recent for the Virgo cluster to have modified their kinematics, we qualitatively interpret the distribution of our sample dEs in the λ_{Re}–age plane as follows. The older ($\gtrsim$5 Gyr) and lower λ_{Re} ($\lesssim$0.4) dEs might have fallen into their previous host group earlier (and/or have been less gas-rich) than the other dEs in our sample. In this way their group environment had enough time to quench their star formation activity (or quenched it faster), and to transform their kinematics to what we have measured. Conversely, the younger dEs in our sample ($\lesssim$5 Gyr) might have been accreted at later times (and/or have been more gas-rich), so that their previous host group was able to transform them to a lesser extent. Their different λ_{Re} values might reflect their different star formation rates, in the sense that a higher star formation rate might yield both a young light-weighted age and a high λ_{Re}, while a low star formation rate might not be sufficient to bear a high λ_{Re}. Additionally, the accretion on to Virgo and the consequent ram pressure of the cluster might have contributed to keep λ_{Re} high by temporarily increasing the star formation rate of the younger dEs in our sample (see Section 5.2).

The two outliers in our sample in Fig. 7 are VCC2019 and VCC0794. It should be noted that VCC2019 shows a star formation history similar to that of VCC0794, after excluding its central nuclear star cluster (Fig. C1 in Appendix C). These two dEs could have formed with high angular momentum, yet low gas reservoir. Hence, their star formation was extinguished either intrinsically or by environmental processes in the group, a long time ago. Alternatively, before being accreted on to a group, these dE could have been quenched in a filament whose density was not high enough to affect their kinematics but adequate to quench their star formation (see Winkel et al. 2021). Both explanations are in agreement with the high [α/Fe] and low [M/H] we estimate for these two dEs (in case of VCC2019, after excluding its nuclear star cluster).

We note that, using the STARLIGHT light-weighted ages for our sample dEs (Table 4) improves their consistency with the λ_{Re}–age relation, without changing our interpretation.

6 CONCLUSION

In this paper, we have investigated the stellar population properties of a sample of nine Virgo dEs that, according to Lisker et al. (2018), have been accreted on to Virgo as gravitationally bound members of a massive galaxy group ($M_\star/M_\odot \sim 10^{13}$) about 2–3 Gyr ago. To this effect, we have developed a four-step fitting routine of spectral indices based on a χ^2 minimization approach, where the observed indices of each galaxy are compared to predictions of SSP models with different age, [M/H], and [α/Fe]. We have applied our fitting routine to the integrated spectra of our sample of dEs, obtained from their MUSE data cubes. Furthermore, we performed full-spectrum fitting (using the STARLIGHT code) to investigate the star formation history of the dEs in our sample. We have compared our results with those for dEs in the Virgo and Coma clusters spanning the same range of galaxy luminosity. The main results of our analysis can be summarized as follows:

(i) Our dEs fall within the age range of 1.85–10.50 Gyr, the metallicity range of $-0.77 <$ [M/H] [dex] < -0.18 and α abundance range of $0.20 <$ [α/Fe] [dex] < 0.43. We obtain a median age of 6.8 ± 1.1 Gyr, median [M/H] of -0.59 ± 0.05 dex, and median [α/Fe] of 0.26 ± 0.02 dex.

(ii) We find our sample dEs to be significantly more α-enhanced (at the 8σ level) and metal-poorer (at the 2-3 σ level) than equally massive dEs of the Virgo and Coma clusters, at similar (or even larger) infall time.

(iii) Six out of nine dEs in our sample show significant peaks in their stellar light and mass fraction distributions between 1 and 4 Gyr ago, at or just after their accretion on to Virgo. These peaks correspond to a 5–30 per cent mass growth, and point to a recent and short episode of star formation, possibly triggered by ram pressure in Virgo. Alternatively it might be due to the intrinsic star formation activity of these galaxies. We speculate that recent and rather short episodes of star formation might be (partly) responsible for the high [α/Fe] abundance ratios in these six dEs. This is consistent with the results of de La Rosa et al. (2011), who showed that galaxies with a short period of star formation (i.e. $\lesssim$2 Gyr) attain higher [α/Fe] values. In the first few tens million years, type-II SNe enrich the interstellar medium (ISM) of α-elements. If star formation lasts less than 1 Gyr (before Type-Ia SNe start to pollute the ISM with Fe), the newly formed stellar population is more enriched in α-elements than Fe, and exhibits high [α/Fe]. If this population is the most recently formed and contributes most of the galaxy light (as the star formation histories in Fig. 5 seem to indicate), then our measurements would actually reflect its [α/Fe]. However, another possible explanation is that the [α/Fe] ratios might mostly arise from the old stellar component in these galaxies, whose star formation activity was quenched on relatively shorter time-scales as the result of pre-processing in the host galaxy group, prior infall into Virgo.

(iv) Our results indicate that the remaining three dEs in our sample (namely VCC0794, VCC1896, and VCC2019) were accreted on to Virgo already quenched. We suggest that their previous host group extinguished their star formation activity before their infall into Virgo. Their relatively high [α/Fe] ratios might thus be the result of quenching due to pre-processing in their previous parent halo.

In this work, we show that knowing the average infall times and star formation histories of recently accreted dEs on to Virgo may allow us to identify galaxies quenched by their previous host halo, thus providing direct proof of group pre-processing. Our results suggest that the combined effect of pre-processing in galaxy groups and environmental effects acting in the early phases of accretion on to a cluster are key drivers of the stellar population properties of low-mass galaxies. In a future work, we will further explore this scenario by analysing the radially resolved stellar population properties of our sample of dEs.

ACKNOWLEDGEMENTS

We acknowledge financial support from the European Union's Horizon 2020 research and innovation program under the Marie Sklodowska-Curie grant agreement no. 721463 to the SUNDIAL ITN network. BB acknowledges the support of the International Max Planck Research School (IMPRS) for Astronomy and Cosmic Physics at the University of Heidelberg. JFB and FLB acknowledges support through the RAVET project by the grant PID2019-107427GB-C32 from the Spanish Ministry of Science, Innovation and Universities (MCIU), and through the IAC project TRACES, which is partially supported through the state budget and the regional budget of the Consejería de Economía, Industria, Comercio y Conocimiento of the Canary Islands Autonomous Community. GvdV acknowledges funding from the European Research Council (ERC) under the European Union's Horizon 2020 research and innovation programme under grant agreement No 724857 (Consolidator Grant ArcheoDyn). The MUSE data cubes used in this work are available in the ESO archive under the ESO programme IDs 098.B-0619 and 0100.B-0573. This research is partially based on data from the MILES project.

DATA AVAILABILITY

Data and results directly referring to content and figures of this publication are available upon request from the corresponding author.

REFERENCES

Bacon R. et al., 2010, in McLean I. S., Ramsay S. K., Takami H., eds, Proc. SPIE Conf. Ser. Vol. 7735, Ground-based and Airborne Instrumentation for Astronomy III. SPIE, Bellingham, p. 773508
Bacon R. et al., 2017, A&A, 608, A1
Balogh M. L., Schade D., Morris S. L., Yee H. K. C., Carlberg R. G., Ellingson E., 1998, ApJ, 504, L75
Bensby T., Feltzing S., Lundström I., 2003, A&A, 410, 527
Bidaran B. et al., 2020, MNRAS, 497, 1904 (B20)

Binggeli B., Sandage A., Tammann G. A., 1988, ARA&A, 26, 509
Boselli A., Gavazzi G., 2006, PASP, 118, 517
Boselli A., Gavazzi G., 2014, A&AR, 22, 74
Boselli A., Fossati M., Sun M., 2022, A&AR, 30, 3
Cardelli J. A., Clayton G. C., Mathis J. S., 1989, ApJ, 345, 245
Carter D. et al., 2008, ApJS, 176, 424
Cenarro A. J. et al., 2007, MNRAS, 374, 664
Cervantes J. L., Vazdekis A., 2009, MNRAS, 392, 691
Chilingarian I. V., Cayatte V., Durret F., Adami C., Balkowski C., Chemin L., Laganá T. F., Prugniel P., 2008, A&A, 486, 85
Cid Fernandes R., Mateus A., Sodré L., Stasińska G., Gomes J. M., 2005, MNRAS, 358, 363
Coenda V., Mast D., Muriel H., Martínez H. J., 2020, A&A, 642, A132
Cole S., Lacey C. G., Baugh C. M., Frenk C. S., 2000, MNRAS, 319, 168
Conroy C., 2013, ARA&A, 51, 393
Davies L. J. M. et al., 2019, MNRAS, 483, 5444
De Rijcke S., Dejonghe H., Zeilinger W. W., Hau G. K. T., 2003, A&A, 400, 119
de La Rosa I. G., La Barbera F., Ferreras I., de Carvalho R. R., 2011, MNRAS, 418, L74
Donnari M. et al., 2021, MNRAS, 500, 4004
Dressler A., 1980, ApJ, 236, 351
Fahrion K. et al., 2021, A&A, 650, A137
Falcón-Barroso J. et al., 2006, MNRAS, 369, 529
Falcón-Barroso J., Sánchez-Blázquez P., Vazdekis A., Ricciardelli E., Cardiel N., Cenarro A. J., Gorgas J., Peletier R. F., 2011, A&A, 532, A95
Falcón-Barroso J. et al., 2019, A&A, 632, A59
Fossati M. et al., 2018, A&A, 614, A57
Fujita Y., 1998, ApJ, 509, 587
Fujita Y., 2004, PASJ, 56, 29
Fujita Y., Nagashima M., 1999, ApJ, 516, 619
Fumagalli M., Gavazzi G., Scaramella R., Franzetti P., 2011, A&A, 528, A46
Gallazzi A., Charlot S., Brinchmann J., White S. D. M., Tremonti C. A., 2005, MNRAS, 362, 41
Gallazzi A., Charlot S., Brinchmann J., White S. D. M., 2006, MNRAS, 370, 1106
Gallazzi A. R., Pasquali A., Zibetti S., Barbera F. L., 2021, MNRAS, 502, 4457
Geha M., Guhathakurta P., van der Marel R. P., 2003, AJ, 126, 1794
Geha M., Guhathakurta P., Rich R. M., Cooper M. C., 2006, AJ, 131, 332
Gonçalves G., Coelho P., Schiavon R., Usher C., 2020, MNRAS, 499, 2327
González Delgado R. M. et al., 2014, ApJ, 791, L16
González Delgado R. M. et al., 2015, A&A, 581, A103
Gunn J. E., Gott J. R. III, 1972, ApJ, 176, 1
Haines C. P. et al., 2015, ApJ, 806, 101
Hester J. A. et al., 2010, ApJ, 716, L14
Janz J., Lisker T., 2008, ApJ, 689, L25
Janz J., Lisker T., 2009, ApJ, 696, L102
Janz J., Salo H., Su A. H., Venhola A., 2021, A&A, 647, A80
Kauffmann G., White S. D. M., Heckman T. M., Ménard B., Brinchmann J., Charlot S., Tremonti C., Brinkmann J., 2004, MNRAS, 353, 713
Kenney J. D. P., Geha M., Jáchym P., Crowl H. H., Dague W., Chung A., van Gorkom J., Vollmer B., 2014, ApJ, 780, 119
Kodama T., Smail I., 2001, MNRAS, 326, 637
Koleva M., de Rijcke S., Prugniel P., Zeilinger W. W., Michielsen D., 2009, MNRAS, 396, 2133
Kormendy J., 1985, ApJ, 295, 73
Kuntschner H. et al., 2006, MNRAS, 369, 497
La Barbera F., Pasquali A., Ferreras I., Gallazzi A., de Carvalho R. R., de la Rosa I. G., 2014, MNRAS, 445, 1977
Larson R. B., Tinsley B. M., Caldwell C. N., 1980, ApJ, 237, 692
Lee B. et al., 2017, MNRAS, 466, 1382
Lewis I. et al., 2002, MNRAS, 334, 673
Lisker T., Grebel E. K., Binggeli B., 2006a, AJ, 132, 497
Lisker T., Glatt K., Westera P., Grebel E. K., 2006b, AJ, 132, 2432
Lisker T., Weinmann S. M., Janz J., Meyer H. T., 2013, MNRAS, 432, 1162
Lisker T., Vijayaraghavan R., Janz J., Gallagher J. S., III, Engler C., Urich L., 2018, ApJ, 865, 40
Liu Y. et al., 2016, ApJ, 818, 179
Mahajan S., Raychaudhury S., Pimbblet K. A., 2012, MNRAS, 427, 1252
Maier C., Ziegler B. L., Haines C. P., Smith G. P., 2019a, A&A, 621, A131
Maier C., Hayashi M., Ziegler B. L., Kodama T., 2019b, A&A, 626, A14
McGee S. L., Balogh M. L., Bower R. G., Font A. S., McCarthy I. G., 2009, MNRAS, 400, 937
Mei S. et al., 2007, ApJ, 655, 144
Michielsen D. et al., 2008, MNRAS, 385, 1374
Mihos J. C., 2004, in Mulchaey J. S., Dressler A., Oemler A., eds, Clusters of Galaxies: Probes of Cosmological Structure and Galaxy Evolution. p. 277 Cambridge University Press
Moore B., Katz N., Lake G., Dressler A., Oemler A., 1996, Nature, 379, 613
Moore B., Lake G., Katz N., 1998, ApJ, 495, 139
Mun J. Y., Hwang H. S., Lee M. G., Chung A., Yoon H., Lee J. C., 2021, J. Korean Astron. Soc., 54, 17
Oemler A., 1974, PhD thesis, California Institute of Technology, Pasadena, California
Oman K. A., Hudson M. J., 2016, MNRAS, 463, 3083
Panter B., Jimenez R., Heavens A. F., Charlot S., 2008, MNRAS, 391, 1117
Pasquali A., Gallazzi A., Fontanot F., van den Bosch F. C., De Lucia G., Mo H. J., Yang X., 2010, MNRAS, 407, 937
Pasquali A., Smith R., Gallazzi A., De Lucia G., Zibetti S., Hirschmann M., Yi S. K., 2019, MNRAS, 484, 1702
Paudel S., Lisker T., Kuntschner H., Grebel E. K., Glatt K., 2010, MNRAS, 405, 800
Peng Y.-j. et al., 2010, ApJ, 721, 193
Penny S. J., Conselice C. J., 2008, MNRAS, 383, 247
Pietrinferni A., Cassisi S., Salaris M., Castelli F., 2004, ApJ, 612, 168
Postman M., Geller M. J., 1984, ApJ, 281, 95
Rhee J., Smith R., Choi H., Yi S. K., Jaffé Y., Candlish G., Sánchez-Jánssen R., 2017, ApJ, 843, 128
Rhee J., Smith R., Choi H., Contini E., Jung S. L., Han S., Yi S. K., 2020, ApJS, 247, 45
Roberts I. D., van Weeren R. J., Timmerman R., Botteon A., Gendron-Marsolais M.-L., Ignesti A., Rottgering H. J. A., 2022, A&A, 658, 14
Ryś A., van de Ven G., Falcón-Barroso J., 2014, MNRAS, 439, 284
Salaris M., Cassisi S., 2005, Evolution of Stars and Stellar Populations. Wiley
Sánchez-Blázquez P. et al., 2006, MNRAS, 371, 703
Sánchez-Blázquez P., Ocvirk P., Gibson B. K., Pérez I., Peletier R. F., 2011, MNRAS, 415, 709
Santos J. S. et al., 2015, MNRAS, 447, L65
Sarzi M. et al., 2006, MNRAS, 366, 1151
Schlafly E. F., Finkbeiner D. P., 2011, ApJ, 737, 103
Scott N. et al., 2020, MNRAS, 497, 1571
Serra P., Trager S. C., 2007, MNRAS, 374, 769
Shen S., Yin J., 2020, in Boquien M., Lusso E., Gruppioni C., Tissera P., eds, Proc. IAU Symp. 341, Panchromatic Modelling with Next Generation Facilities. Kluwer, Dordrecht, p. 147
Smith R. J., Lucey J. R., Hudson M. J., Allanson S. P., Bridges T. J., Hornschemeier A. E., Marzke R. O., Miller N. A., 2009, MNRAS, 392, 1265
Smith R., Pacifici C., Pasquali A., Calderón-Castillo P., 2019, ApJ, 876, 145
Steyrleithner P., Hensler G., Boselli A., 2020, MNRAS, 494, 1114
Su A. H. et al., 2021, A&A, 647, A100
Sybilska A. et al., 2017, MNRAS, 470, 815
Sybilska A., Kuntschner H., van de Ven G., Vazdekis A., Falcón-Barroso J., Peletier R. F., Lisker T., 2018, MNRAS, 476, 4501
Şen Ş. et al., 2018, MNRAS, 475, 3453
Thomas D., Greggio L., Bender R., 1999, MNRAS, 302, 537
Thomas D., Maraston C., Bender R., 2003, MNRAS, 339, 897
Thomas D., Maraston C., Bender R., Mendes de Oliveira C., 2005, ApJ, 621, 673
Tiwari J., Mahajan S., Singh K. P., 2020, New Astron., 81, 101417
Toloba E., Boselli A., Cenarro A. J., Peletier R. F., Gorgas J., Gil de Paz A., Muñoz-Mateos J. C., 2011, A&A, 526, A114
Toloba E. et al., 2014, ApJS, 215, 17

Trager S. C., Worthey G., Faber S. M., Burstein D., González J. J., 1998, ApJS, 116, 1
Trager S. C., Worthey G., Faber S. M., Dressler A., 2005, MNRAS, 362, 2
Trussler J., Maiolino R., Maraston C., Peng Y., Thomas D., Goddard D., Lian J., 2021, MNRAS, 500, 4469
Vazdekis A., Casuso E., Peletier R. F., Beckman J. E., 1996, ApJS, 106, 307
Vazdekis A., Sánchez-Blázquez P., Falcón-Barroso J., Cenarro A. J., Beasley M. A., Cardiel N., Gorgas J., Peletier R. F., 2010, MNRAS, 404, 1639
Vazdekis A. et al., 2015, MNRAS, 449, 1177
van Zee L., Skillman E. D., Haynes M. P., 2004, AJ, 128, 121
Venhola A. et al., 2021, preprint (arXiv:2111.01855)
Vijayaraghavan R., Gallagher J. S., Ricker P. M., 2015, MNRAS, 447, 3623
Vincenzo F., Weinberg D. H., Miglio A., Lane R. R., Roman-Lopes A., 2021, MNRAS, 508, 5903
Vollmer B., Cayatte V., Balkowski C., Duschl W. J., 2001, ApJ, 561, 708
Walcher C. J., Coelho P., Gallazzi A., Charlot S., 2009, MNRAS, 398, L44
Wetzel A. R., Tinker J. L., Conroy C., van den Bosch F. C., 2013, MNRAS, 432, 336
Wheeler C., Phillips J. I., Cooper M. C., Boylan-Kolchin M., Bullock J. S., 2014, MNRAS, 442, 1396
Wheeler C. et al., 2017, MNRAS, 465, 2420
Whitmore B. C., Gilmore D. M., Jones C., 1993, ApJ, 407, 489
Winkel N., Pasquali A., Kraljic K., Smith R., Gallazzi A., Jackson T. M., 2021, MNRAS, 505, 4920
Zoldan A., De Lucia G., Xie L., Fontanot F., Hirschmann M., 2018, MNRAS, 481, 1376

APPENDIX A: LIST OF INDEX BAND PASSES

Table A1. List of indices used in this study.

Index	Blue bandpass (Å)	Central bandpass (Å)	Red bandpass (Å)	Reference
H β	4827.875–4847.875	4847.875–4876.625	4876.625–4891.625	(Trager et al. 1998)
H β_o	4821.175–4838.404	4839.275–4877.097	4897.445–4915.845	(Cervantes & Vazdekis 2009)
Fe5015	4946.500–4977.750	4977.750–5054.000	5054.000–5065.2500	(Trager et al. 1998)
Mgb5177	5142.625–5161.375	5160.125–5192.625	5191.375–5206.375	(Trager et al. 1998)
Fe5270	5233.150–5248.150	5245.650–5285.650	5285.650–5318.150	(Trager et al. 1998)
Fe5335	5304.625–5315.875	5312.125–5352.125	5353.375–5363.375	(Trager et al. 1998)

Note. The columns show: index's name, its corresponding blue pseudo-continuum, main absorption feature, red pseudo-continuum, and the reference where the index was defined.

In Table A1, we provide the list of Lick indices used in this study.

APPENDIX B: LICK INDICES VERSUS STARLIGHT FITTING

In Fig. B1, we compare the results of STARLIGHT (Table 4) with those from the Lick indices fitting (Table 2). In the top panel of this figure,

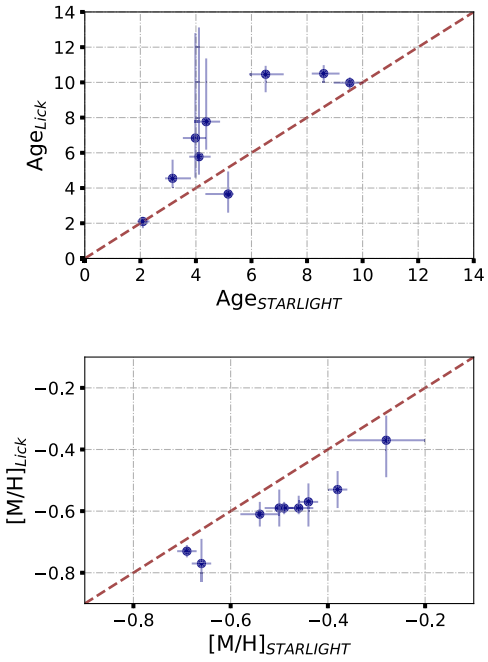

Figure B1. *Top panel*: Comparing light-weighted age values obtained from STARLIGHT full spectrum fitting (x-axis) with those derived through Lick indices fitting (y-axis). The data points represent dEs in our sample. *Bottom panel*: Same comparison as the top panel but for light-weighted [M/H] values.

we compare the light-weighted mean ages obtained from STARLIGHT (on the *x*-axis) and the average ages derived by fitting over Lick indices (on the *y*-axis). A similar comparison, but for light-weighted mean [M/H], is presented in the bottom panel. A KS-test applied to these two sets shows that the two fitting methods are generally consistent, with *p*-value = 0.35 and 0.12 for age and metallicity, respectively).

B1 shows that STARLIGHT generally underestimates age and overestimates metallicity with respect to Lick indices. This can partly be due to systematic and fundamental differences between the two fitting methods. STARLIGHT considers a mixture of SSP models to construct the best-fitting model. Thus, for galaxies with multiple epochs of star formation, STARLIGHT provides a more realistic approach than the Lick indices fitting based on one SSP. Precisely, the light-weighted age and [M/H] in Table 4 are derived with STARLIGHT by accounting for the possible contribution of both young and old SSPs in the observed spectrum, whereas in Table 2, we base our Lick indices analysis solely on one SSP without simultaneously considering different SSP components.

In Section 3.4, we state that STARLIGHT accepts only a maximum number of 300 SSPs, while for the Lick indices fitting, such limitation does not exist (we use $\sim$ 2410 000 SSP models). Hence, STARLIGHT determines the best-fitting spectrum based on a limited model space that has uneven spacing in the [M/H] axis and a spacing of 1 Gyr in the age axis. This may affect the contribution of each SSP model to the best-fitting spectrum, thus the final average values of age and [M/H]. It should also be noted that the uncertainties due to model degeneracies (particularly for models older than 6 Gyr) is still relevant for the results of the full-spectrum fitting. In addition, the results of the Lick indices fitting noticeably suffer from the well-known issue of the 'age–metallicity degeneracy'. According to Sánchez-Blázquez et al. (2011), this issue is less relevant for full-spectrum fitting, yet it should be taken into account while interpreting the present discrepancy between the results of these two approaches.

APPENDIX C: THE EFFECTS OF THE NUCLEAR STAR CLUSTER IN VCC0990 AND VCC2019

Table C1. Integrated light-/mass-weighted stellar population properties of dEs with NSC.

Object	R_{NSC} (arcsec)	$<Age>_L$ (Gyr)	$<[M/H]>_L$ (dex)	$<Age>_M$ (Gyr)	$<[M/H]>_M$ (dex)
VCC0990	3.2	5.76 ± 0.43	-0.49 ± 0.11	6.54 ± 0.50	-0.45 ± 0.10
VCC2019	3.9	8.27 ± 0.85	-0.55 ± 0.15	8.48 ± 0.85	-0.51 ± 0.13

Note. The columns show: Columns are: name of the target, NSC radius, galaxy's light-weighted age, light-weighted metallicity, mass-weighted age, and mass-weighted metallicity.

We investigate how the inferred star formation history, age, and [M/H], of VCC0990 and VCC2019 change after excluding their central nuclear star cluster (NSC). To reliably estimate the NSC size, we first discard spaxels with S/N < 3 and then sum each dE's MUSE data cube along the wavelength axis, between 4750 and 5540 Å. This is the exact wavelength range over which we performed STARLIGHT fitting in Section 3.4. We then stack all the rows of the resulting image to construct the light distribution of the entire galaxy, which we simultaneously fit with two Gaussian functions, one with a broad kernel for the diffuse galaxy, and the other with a narrow kernel for the galaxy's NSC. We adopt the FWHM of the best-fitting narrow Gaussian as the size of the NSC, whose value is reported in Table C1 for each of the two galaxies. We then exclude the spaxels in the central area of the galaxy as defined by its NSC radius, and construct a new integrated MUSE spectrum for each galaxy. We fit both spectra using STARLIGHT as described in Section 3.4, and report the resulting light- and mass-weighted age and [M/H] in Table C1. The exclusion of most of the NSC emission from their integrated spectra turns VCC0990 and VCC2019 older (at the 1.7σ level) and slightly metal-poorer (at the 1σ level). As stated in Section 4.3 the presence of a young NSC in the core of VCC0990 and VCC2019 leverages the contribution of young SSPs in the STARLIGHT best fit.

The light and mass fractions of VCC0990 and VCC2019, before and after excluding their NSC, are traced in Fig. C1 as a function of time. Their corresponding cumulative mass distributions are shown in Fig. C2. The peak at younger ages (i.e. at $\sim$2 Gyr for VCC0990 and $\sim$4 Gyr for VCC2019) in the star formation history of these two dEs is noticeably reduced after excluding their NSC from their integrated spectra. This indicates that VCC2019 was quenched mostly before its accretion on to the Virgo cluster. According to Fig. C1, the star formation activity of VCC0990 continued even after its accretion on to the Virgo cluster. Nevertheless, this phase of star formation corresponds to less than 10 per cent stellar mass growth (as shown in Fig. C2), and it might be due to possible residual NSC emission in the galaxy's integrated spectrum.

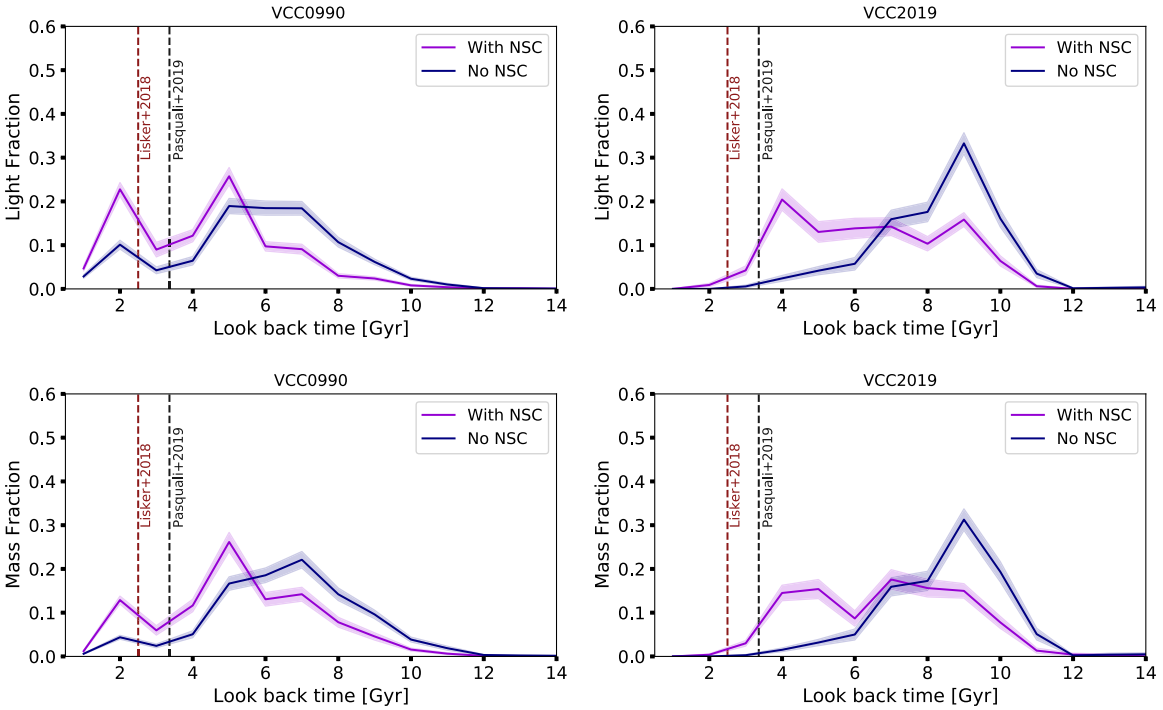

Figure C1. Similar to Fig. 5 but only for VCC0990 (left-hand panels) and VCC2019 (right-hand panels). In each panel, the light and mass fractions before and after excluding the NSC are traced with purple and blue, respectively.

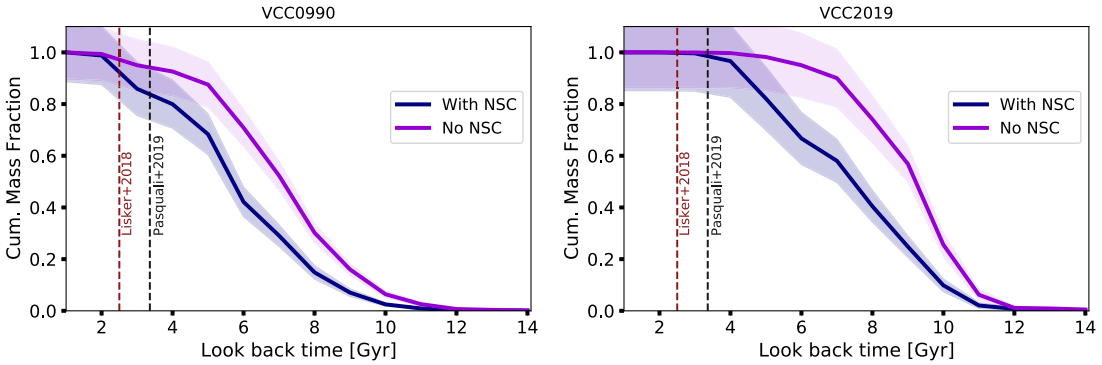

Figure C2. Similar to Fig. 6 but only for VCC0990 (left-hand panel) and VCC2019 (right-hand panel). Similar to Fig. C1 the light and mass fractions before and after excluding the NSC are traced with purple and blue, respectively.

This paper has been typeset from a TEX/LATEX file prepared by the author.